

Lee J. Styslinger Jr.
College of Engineering

PROJECT NUMBER: ALDOT 930-972

CONDITION ASSESSMENT OF STEEL BOX GIRDER BRIDGE USING LONG-TERM FIELD MEASUREMENTS

FINAL REPORT

By

Hannah D. Kessler, Ph.D.

Wei Song, Ph.D.

Tulsiram Bhattarai

Carlos Andres Canchila Martinez

Mohammad Javad Masoudi

Mohammed Yusuf Mujawar

Department of Civil, Construction and Environmental Engineering

Styslinger College of Engineering

The University of Alabama

for

Alabama Department of Transportation

Montgomery, Alabama

August 2026

TECHNICAL REPORT DOCUMENTATION PAGE

1. Report No. 930-972	2. Government Accession No.	3. Recipient's Catalog No.	
4. Title and Subtitle Condition Assessment of Steel Box Girder Bridge Using Long-Term Field Measurements		5. Report Date August 2026	
		6. Performing Organization Code:	
7. Author(s) Hannah D. Kessler, Ph.D. (ORCID: 0000-0002-6135-350X); Wei Song, Ph.D.; Tulsiram Bhattarai (ORCID: 0009-0002-7017-4930); Carlos Canchila (ORCID: 0009-0002-8952-6297); Mohammad Javad Masoudi (ORCID: 0000-0002-4848-6164); Mohammed Yusuf Mujawar		8. Performing Organization Report No.	
9. Performing Organization Name and Address The University of Alabama 152 Rose Administration Box 870104 Tuscaloosa, AL, 35487-0104		10. Work Unit No.	
		11. Contract or Grant No.	
12. Sponsoring Agency Name and Address Alabama Department of Transportation 1409 Coliseum Blvd Montgomery, AL 36130		13. Type of Report and Period	
		14. Sponsoring Agency Code	
15. Supplementary Notes			

16. Abstract

The evaluation of the structural condition and fatigue performance of the I-20/59 McFarland Bridge, Alabama's first arch-rib stiffened steel box girder bridge, was performed using long-term field monitoring and finite element (FE) model updating. More than 2,000 acceleration records were measured between October 2025 and February 2026 using an automated monitoring system equipped with accelerometers. The bridge's dynamic characteristics were identified using operational modal analysis, and the results were used for FE model updating. The updated model showed good agreement with measured modal properties and was subsequently used for the assessment of fatigue-sensitive details under AASHTO fatigue truck loading. Thirteen fatigue-critical details were investigated, and the predicted stress ranges for all considered locations were below the corresponding constant amplitude fatigue thresholds, indicating infinite fatigue life. The results indicate that the bridge is not currently prone to load-induced fatigue damage and this report provides ALDOT with an experimentally validated framework for future bridge monitoring, assessment, and asset management.

17. Key Words Steel box girder bridge, fatigue, field monitoring, model updating	18. Distribution Statement No restrictions.		
19. Security Classif. (of this report) Unclassified	20. Security Classif. (of this page) Unclassified	21. No. of Pages 56	22. Price None

SI* (MODERN METRIC) CONVERSION FACTORS

APPROXIMATE CONVERSIONS TO SI UNITS

Symbol	When You Know	Multiply By	To Find	Symbol
		LENGTH		
in	inches	25.4	millimeters	mm
ft	feet	0.305	meters	m
yd	yards	0.914	meters	m
mi	miles	1.61	kilometers	km
		AREA		
in^2	square inches	645.2	square millimeters	mm^2
ft^2	square feet	0.093	square meters	m^2
yd^2	square yard	0.836	square meters	m^2
ac	acres	0.405	hectares	ha
mi^2	square miles	2.59	square kilometers	km^2
		VOLUME		
fl oz	fluid ounces	29.57	milliliters	mL
gal	gallons	3.785	liters	L
ft^3	cubic feet	0.028	cubic meters	m^3
yd^3	cubic yards	0.765	cubic meters	m^3
		NOTE: volumes greater than 1000 L shall be shown in m^3		
		MASS		
oz	ounces	28.35	grams	g
lb	pounds	0.454	kilograms	kg
T	short tons (2000 lb)	0.907	megagrams (or "metric ton")	Mg (or "t")
		TEMPERATURE (exact degrees)		
°F	Fahrenheit	5 (F-32)/9 or (F-32)/1.8	Celsius	°C
		ILLUMINATION		
fc	foot-candles	10.76	lux	lx
fl	foot-Lamberts	3.426	candela/m^2	cd/m^2
		FORCE and PRESSURE or STRESS		
lbf	poundforce	4.45	newtons	N
lbf/in^2	poundforce per square inch	6.89	kilopascals	kPa

APPROXIMATE CONVERSIONS FROM SI UNITS

Symbol	When You Know	Multiply By	To Find	Symbol
		LENGTH		
mm	millimeters	0.039	inches	in
m	meters	3.28	feet	ft
m	meters	1.09	yards	yd
km	kilometers	0.621	miles	mi
		AREA		
mm^2	square millimeters	0.0016	square inches	in^2
m^2	square meters	10.764	square feet	ft^2
m^2	square meters	1.195	square yards	yd^2
ha	hectares	2.47	acres	ac
km^2	square kilometers	0.386	square miles	mi^2
		VOLUME		
mL	milliliters	0.034	fluid ounces	fl oz
L	liters	0.264	gallons	gal
m^3	cubic meters	35.314	cubic feet	ft^3
m^3	cubic meters	1.307	cubic yards	yd^3
		MASS		
g	grams	0.035	ounces	oz
kg	kilograms	2.202	pounds	lb
Mg (or "t")	megagrams (or "metric ton")	1.103	short tons (2000 lb)	T
		TEMPERATURE (exact degrees)		
°C	Celsius	1.8C+32	Fahrenheit	°F
		ILLUMINATION		
lx	lux	0.0929	foot-candles	fc
cd/m^2	candela/m^2	0.2919	foot-Lamberts	fl
		FORCE and PRESSURE or STRESS		
N	newtons	0.225	poundforce	lbf
kPa	kilopascals	0.145	poundforce per square inch	lbf/in^2

TABLE OF CONTENTS

DISCLAIMERS ..... **XII**

CHAPTER 1 - EXECUTIVE SUMMARY **1**

CHAPTER 2 - INTRODUCTION **3**

2.1 BACKGROUND AND MOTIVATION 3
2.2 DESCRIPTION OF THE I-20/59 MCFARLAND BRIDGE 4
2.3 RESEARCH OBJECTIVES AND SCOPE 4
2.4 PROJECT OUTCOMES AND DELIVERABLES 4
2.5 REPORT OUTLINE 5

CHAPTER 3 - LITERATURE REVIEW **6**

3.1 FATIGUE OF STEEL BRIDGE COMPONENTS 6
3.2 AASHTO FATIGUE PROVISIONS 7
3.3 FATIGUE OF STEEL BOX GIRDERS 9

CHAPTER 4 - METHODS **11**

4.1 DATA COLLECTION SYSTEM 11
4.1.1 BDI System 11
4.1.2 Data Collection and Transmission 13
4.2 VIBRATION MODAL ANALYSIS 15

CHAPTER 5 - I-20/59 AND MCFARLAND BRIDGE **17**

5.1 BRIDGE OVERVIEW 17
5.1.1 General Overview 17
5.1.2 Instrumentation Plan 21
5.2 DATA 23
5.2.1 Accelerometer Data 23
5.2.2 Vibration Modal Analysis 25

CHAPTER 6 - FINITE ELEMENT MODELING FRAMEWORK **28**

6.1 OVERVIEW 28
6.2 GEOMETRY 28
6.3 MATERIAL PROPERTIES 29
6.4 BOUNDARY CONDITIONS 30
6.5 INTERACTIONS 34
6.6 MESH 35
6.7 LOCAL COORDINATE SYSTEMS 36
6.8 FINITE ELEMENT MODEL UPDATING 37
6.8.1 Selection of modes for Comparison 38
6.8.2 Selection of Updating Parameters 38
6.8.3 Model Updating Criteria 39
6.8.4 Selection of the Updated Model 40
6.8.5 Natural Frequencies and Mode Shapes 41

CHAPTER 7 - FATIGUE LIFE ESTIMATION **43**

7.1 FATIGUE LOADING 43
7.2 FATIGUE SENSITIVE DETAILS 45
7.3 FATIGUE LIFE ESTIMATION 50

CHAPTER 8 - CONCLUSIONS AND RECOMMENDATIONS 53
8.1 CONCLUSIONS 53
8.2 IMPLEMENTATION FOR ALDOT 53
8.3 FUTURE RESEARCH 54
ACKNOWLEDGEMENTS 55
REFERENCES 56

LIST OF FIGURES

Figure 1. Characteristics of the AASHTO HL-93 design truck [6]. 7
Figure 2. S-N curves for different detail categories [6]. 8
Figure 3. Photos and relative location of data logger cabinet. 12
Figure 4. Photos of data logger, 4- and 16-channel terminal nodes, and an accelerometer 12
Figure 5. Stabilization diagram overlapped with the normalized PSD. Red vertical lines indicate stable, physical modes identified across a set of candidates. 16
Figure 6. Framing plan of the arch bridge superstructure. 18
Figure 7. Elevation view of the arch rib and hanger system. 19
Figure 8. Typical cross section of the bridge illustrating the deck width, girder arrangement, and transverse geometry. 19
Figure 9. Typical girder cross-sectional details showing the geometry and dimensions of the steel box girder components. 20
Figure 10. Arch rib cross-sectional details showing the geometry and dimensions of the steel box section. 20
Figure 11. Instrumentation layout and photos of accelerometer installed on a girder and an arch. 22
Figure 12. Days when data was collected (marked in green) from October 2025 to February 2026 24
Figure 13. Typical five minute vibration record from sensors installed on the girders. 24
Figure 14. Typical five minute vibration record from sensors installed on the arches. 25
Figure 15. Distribution of identified natural frequencies with clustered (shadowed) regions 26
Figure 16. The first three modes identified from modal analysis of the experimental data. 27
Figure 17. Complete finite-element model of the tied-arch bridge. 29
Figure 18. Layout of the I-20/59 bridge showing abutments, bearings, longitudinal girders, transverse floor beams, and arch ribs. 30
Figure 19. Bearing layout and support designations at girder ends. 31
Figure 20. Bearing boundary conditions: (a) specialized roller support (R) for girders 1 and 7; (b) non-guided expansion (NE) bearing for girders 2, 3, 5, and 6 32
Figure 21. Arch rib anchorage details from the shop drawings, showing the base plate, anchor rods, and supporting system. 34
Figure 22. Perspective view of the finite element mesh for girders, floor beams, and arches. 36

Figure 23. Representative local coordinate systems assigned to the shell surfaces for stress evaluation, along with the global coordinate system. 37
Figure 24. First nine vibration mode shapes obtained from the Abaqus eigenvalue analysis. 42
Figure 25. Fatigue loading scenarios adopted to maximize the stress response at different stress measurement points. 44
Figure 26. Global load positions on main girder 4. 45
Figure 27. Load location A. 46
Figure 28. Details of stress points from load location A. 47
Figure 29. Load location B. 47
Figure 30. Details of stress points from load location B. 48
Figure 31. Load location C. 49
Figure 32. Details of stress points from load location C. 49
Figure 33. Load location D. 50
Figure 34. Details of stress points from load location D. 50
Figure 35. Location of maximum stress point. 52
Figure 36. Detail of maximum stress point at the connection of floor beam 5 and main girder 7. 52

LIST OF TABLES

Table 1. Fatigue detail category constants from AASHTO LRFD BDS. 9
Table 2. Summary of installed accelerometers with measurement direction and location. 23
Table 3. Material properties used in the finite element model. 30
Table 4. Summary of finite element boundary condition constraints at girder supports. 32
Table 5. Summary of finite element model updating results. 40
Table 6. Modal properties of the final updated finite element model. 41
Table 7. Fatigue design truck wheel loads and applied contact pressures. 43
Table 8. Identified fatigue sensitive details. 46
Table 9. Summary of maximum stress values. 51

LIST OF ABBREVIATIONS AND SYMBOLS

A	constant specific to detail category
AASHTO	American Association of State Highway and Transportation Officials
ADT	average daily traffic
$ADTT$	average daily truck traffic
$(ADTT)_{SL}$	single-lane ADTT
ALDOT	Alabama Department of Transportation
AM	Ante Meridiem
ASTM	American Society for Testing and Materials
BDI	Bridge Diagnostics, Inc.
BDS	Bridge Design Specifications
CAE	computer aided engineering
CAFT	constant amplitude fatigue threshold
CG	center of gravity
CPU	central processing unit
DAQ	data acquisition
DOF	degrees of freedom
E	modulus of elasticity
E_c	elastic modulus of concrete
ERA	eigensystem realization algorithm
E_s	elastic modulus of steel
FE	finite element
fe	frequency error
FEA	finite element analysis
FEM	finite element method
f_i^{FE}	numerical natural frequencies of mode i
f_i^{EXP}	experimental natural frequencies of mode i
ft	feet
g	acceleration due to gravity
GB	gigabyte
GEL	longitudinally guided expansion bearing

GHz	gigahertz
IM	vehicular dynamic load allowance
in	inch
IPS	inch-pound-second
ITS	intelligent transportation systems
J	objective function value
HL	highway load
Hz	hertz
k_c	elastic modulus scaling factor for concrete deck
kg	kilogram
kip	kilopound
k_s	elastic modulus scaling factor for steel components
ksi	kilopound per square inch
LRFD	load and resistance factor design
m	fatigue growth constant
MAC	modal assurance criteria
MPC	multipoint constraints
n	number of stress range cycles per truck passage
N	number of cycles to failure
N_m	number of modes
NAS	network-attached storage
NE	non-guided expansion bearing
NExT	natural excitation technique
NSTM	nonredundant steel tension member
OMA	operational modal analysis
p	fraction of traffic in a single lane
PM	post meridiem
PSD	power spectral density
psi	pound per square inch
R	rotational degree of freedom
RAC	Research Advisory Committee

RAM	random access memory
RP	reference point
S	second
SHM	structural health monitoring
SN	stress-life
SRM	system redundant member
STS	structural testing system
TB	terabyte
TDMS	technical data management streaming
U	translational degree of freedom
UR	translational and rotational degree of freedom
USA	United States of America
VP	Vice President
$(\Delta F)_n$	nominal stress range
$(\Delta F)_{TH}$	constant-amplitude fatigue threshold (CAFT)
ρ	mass density
ν	Poisson's ratio
ψ_i^{EXP}	experimental mode shape vector
$\psi_i(\alpha)$	numerical mode shape vector

DISCLAIMERS

The contents of this report reflect the views of the author(s) who is (are) responsible for the facts and the accuracy of the data presented herein. The contents do not necessarily reflect the official views or policies of the State of Alabama, Alabama Department of Transportation or the Federal Highway Administration. This report does not constitute a standard, specification, or regulation. Comments contained in this paper related to specific testing equipment or materials are not considered an endorsement of any commercial product(s) and/or service(s): no such endorsement is intended or implied.

Hannah D. Kessler, Ph.D.

Research Supervisor

CHAPTER 1 - EXECUTIVE SUMMARY

The I-20/59 McFarland Bridge in Tuscaloosa is the first arch-rib stiffened steel box girder bridge constructed in Alabama. As steel box girder bridges contain several complex bolted and welded connections, evaluating the long-term structural performance is important for ensuring safe operation. To support ALDOT's bridge management efforts, Project 930-972 was undertaken to assess the fatigue vulnerability of the bridge using field monitoring and advanced numerical modeling.

The primary objectives of the project were to conduct long-term field monitoring of the bridge, develop and update a finite element model using the measured structural dynamic response, and evaluate the fatigue performance of fatigue-sensitive details present in the bridge. To achieve these objectives, a long-term monitoring system consisting of 9 accelerometers connected to a Bridge Diagnostics, Inc. (BDI) data acquisition system was installed on the bridge. The monitoring system collected acceleration data between October 2025 and February 2026. More than 2,000 acceleration records were collected using an automated acquisition and transmission system.

Operational modal analysis (OMA) techniques based on the natural excitation technique (NExT) and eigensystem realization algorithm (ERA) were used to analyze the recorded acceleration data. The analysis identified the bridge's dominant vibration characteristics, including natural frequencies and mode shapes. Three primary vibration modes were consistently identified at frequencies of approximately 1.45 Hz, 2.55 Hz, and 3.06 Hz. These experimentally identified modal properties were used as the basis for finite element modal updating.

A detailed finite element model of the bridge was developed in ABAQUS using design and shop drawings provided by ALDOT. The model included the bridge deck, steel box girders, floor beams, arch ribs, hangers, support conditions and structural interactions. Material and interaction properties were adjusted for modal updating until agreement between the numerical and experimentally identified modal characteristics was achieved.

The final updated model maintained the nominal steel elastic modulus, reduced the concrete deck elastic modulus to 60% of its nominal value, and assumed full composite interaction between the steel superstructure and concrete deck. The updated model achieved frequency errors of 3.59%, 3.75%, and 4.95% for the three selected modes, while producing modal assurance criterion (MAC) values of 0.9882, 0.9648, and 0.9300, indicating excellent agreement between measured and calculated mode shapes.

The fatigue life of the bridge was predicted using the updated finite element model following the provisions of the AASHTO LRFD Bridge Design Specifications. Thirteen fatigue-sensitive details, including bolted and welded connections, diaphragm openings, splice regions, and girder-to-floor beams connections, were selected and evaluated. Fatigue loading was represented using the AASHTO fatigue design truck positioned to maximize stresses at each detail.

Results from the fatigue performance assessment show that all considered details experience stress ranges significantly below their corresponding constant amplitude fatigue threshold (CAFT). Consequently, all investigated details are predicted to have infinite fatigue life based on the AASHTO load-induced fatigue provisions. A supplementary review of maximum stresses throughout the bridge also confirmed that the most highly stressed location remains below the applicable fatigue threshold.

Based on the field monitoring, model updating, and fatigue performance assessment completed as part of this project, the I-20/59 McFarland Bridge is not predicted to be susceptible to load-induced fatigue damage under current traffic conditions. The bridge is expected to provide satisfactory long-term performance from the standpoint of fatigue damage.

In addition to the prediction of fatigue life of the bridge, the project produced several valuable deliverables for ALDOT such as a long-term bridge monitoring database containing more than 2,000 vibration records, an experimentally validated finite element model suitable for future analysis and evaluation, and recommendations for future monitoring, inspection, and research activities.

Future work should focus on re-instrumenting the arch ribs to improve characterization of arch vibration modes, installing strain gauges at selected fatigue-sensitive locations to directly measure stress ranges, extending long-term monitoring efforts, and periodically reassessing fatigue performance as traffic patterns evolve. The monitoring and model-updating methodology developed in this project can also serve as a framework for evaluating other critical bridges with similar structural characteristics.

CHAPTER 2 - INTRODUCTION

2.1 BACKGROUND AND MOTIVATION

The use of steel box girders in bridge construction has increased in the United States since the late 1990s [1]. This growth is driven by several of the advantages of box girders, including enhanced structural performance, durability, and favorable aesthetics. Steel box girders provide high rotational stiffness, making them well suited for bridges subjected to significant torsional demands, such as long spans and curved interchange ramps. The box geometry reduces the number of exposed bracing components that would otherwise be prone to debris accumulation and corrosion. Additionally, increased implementation of box girders by bridge designers can also be attributed to their clean form and appearance.

Steel box girders were first introduced into the American Association of State Highway and Transportation Officials (AASHTO) Standard Specification for Highway Bridges in the early 1970s, with earlier field applications dating to the 1960s [2]. As design methodologies have evolved, the cross-sectional form of box girders has transitioned from fully closed steel boxes fabricated with four steel plate sides to partially closed trapezoidal tub girders. Modern tub girder systems typically consist of steel webs and bottom flanges, with top flanges connected compositely to a concrete deck that closes the section.

Despite their advantages, steel box girder bridge systems still face several technical challenges. First, because box girder bridges typically require fewer primary load-bearing members than comparable I-girder systems, structural redundancy is a concern. The failure of a limited number of critical components may have a disproportionate impact on overall system performance. As a result, condition assessment and fatigue evaluation in the field are of particular importance for bridge owners.

Second, steel box girder bridges rely on a system of internal and external cross-frames, diaphragms, and flange lateral bracing to ensure stability during erection, deck casting, and in-service conditions. The connection details associated with these components have complex stress distributions and may be prone to fatigue damage. This complexity is further amplified by common bridge design features such as long or curved spans and skewed supports.

Finally, the basic design requirements and analysis methodologies for several key structural components of steel box girder bridges are not as well established as those for more conventional bridge systems [1]. Accurately characterizing stress demands in fatigue-critical regions remains challenging. These challenges underscore the need for field-based data and refined numerical models to support fatigue evaluation and long-term performance assessment.

2.2 DESCRIPTION OF THE I-20/59 MCFARLAND BRIDGE

The construction of an arch-rib stiffened steel box girder bridge was finished in 2021 in Tuscaloosa County as part of a bridge replacement to carry traffic from I-20/59 over McFarland Boulevard. This marked the first time that this type of bridge was built in the state of Alabama. The bridge consists of seven steel box girders and two steel arch ribs. Each box girder spans 250 ft and is supported by bearings at both ends with a skew angle of 20.5°. The I-20/59 McFarland bridge incorporates many of the defining characteristics and challenges associated with modern steel box girder bridges previously discussed. Given its significance as a first-of-its-kind structure in Alabama and its role in a heavily trafficked interstate corridor, ensuring the I-20/59 McFarland bridge's satisfactory long-term fatigue performance and continued safe operation is of critical importance to the Alabama Department of Transportation (ALDOT)

2.3 RESEARCH OBJECTIVES AND SCOPE

The primary objective of this research project was to provide the ALDOT Bridge Bureau with a rigorous assessment of the fatigue vulnerability of the I-20/59 McFarland bridge based on field measurements and numerical modeling. The results and assessment contained herein will support informed decision-making regarding the bridge's long-term operations, while also generating valuable knowledge applicable to the design, evaluation, and maintenance of similar steel box girder bridges nationwide.

The specific tasks of the project included the following:

1. Conducting a long-term monitoring program to obtain field measurements.
2. Developing a refined finite element (FE) model of the bridge and update using field acceleration measurements.
3. Evaluating the fatigue life of details present on the bridge using the updated FE model.
4. Producing a comprehensive report summarizing the results of Tasks 1 through 3 and offering recommendations to ALDOT and directions for future research.

2.4 PROJECT OUTCOMES AND DELIVERABLES

The primary objective of this research project was to provide the ALDOT Bridge Bureau with an assessment of the fatigue vulnerability of the I-20/59 McFarland bridge using field measurements. The assessment results validate the current safety of the bridge and provide valuable insights for the design and operation of similar steel box girder bridges nationwide. The key deliverables developed from this project include:

i. A fatigue demand assessment and associated fatigue life prediction for the I-20/59 McFarland to support ALDOT asset management and decision-making.

ii. A refined and updated finite element model of the I-20/59 McFarland bridge to support future advanced analyses.

iii. Provide recommendations to the ALDOT Bridge Bureau for future monitoring and research efforts.

2.5 REPORT OUTLINE

This report is organized as follows. Chapter 1 provides an executive summary of the research report. Chapter 2 introduces the research background, objectives, and deliverables. Chapter 3 contains a review of the state-of-the-art for fatigue of steel bridge components and finite element model updating. Chapter 4 reports the methods used for this project, including the data collection system and calculation algorithms. Chapter 5 provides an overview of the I-20/59 McFarland bridge, the instrumentation plan, and the data collected from the bridge. Chapter 6 reviews the finite element modeling and updating framework. Chapter 7 lists the fatigue-sensitive details present on the bridge and projects their fatigue lives based on the updated finite element model. Chapter 8 provides conclusions and recommendations for future work.

CHAPTER 3 - LITERATURE REVIEW

3.1 FATIGUE OF STEEL BRIDGE COMPONENTS

Bridges are subjected to repeated and varying loads due to moving traffic during their service life. Under such loading conditions, cracks can initiate and propagate, causing progressive damage to the bridge components, a phenomenon known as fatigue. Over the life of a bridge, this progressive damage can cause brittle failure even when the applied cyclic stress is well below the yield stress if the structure is not properly designed and monitored [3].

Fatigue has been recognized as one of the most critical deterioration mechanisms in steel bridges, as cracks that initiate and propagate due to repeated loading can compromise structural serviceability and integrity. Although substantial research has been performed to assess the fatigue life of components in a laboratory setting, the accurate evaluation of fatigue damage and reliable prediction of the remaining fatigue life of steel bridge components in the field remains challenging [4]. This is due to stochastic nature of traffic loading, uncertainties in material behavior, and the complexity of fatigue crack initiation and propagation.

Fatigue damage of steel bridges can lead to interruption of regular traffic service or even catastrophic collapse of bridges, such as the Point Pleasant Bridge in the United States in 1967 [3], the Fujigawa Bridge in Japan in 1975 [5] and the Sungsoo Grand Bridge in South Korea in 1994 [5]. In steel bridges, several connections are prone to fatigue damage, including welded and bolted connections, flange to web joints, transverse stiffeners, and diaphragm connections, due to stress concentration in these regions arising from geometric discontinuities. Welded details are particularly susceptible to fatigue damage because of local geometric discontinuities and residual stresses introduced during fabrication [3].

Fatigue behavior is typically categorized as either load-induced and distortion-induced [6]. Load-induced fatigue damage generally occurs due to the repetitive application of cyclic loads, primarily vehicular traffic in bridges. The primary cause of distortion-induced fatigue occurs when the deflection of bridge components differ relative to the attached components and secondary stresses are generated. In bridges, secondary stresses are produced by unevenly applied vehicular traffic loads, which cause secondary deformation [7].

While load-induced fatigue is regarded as a loading issue, distortion-induced fatigue primarily results from stiffness effects. It is relatively straightforward to design structural details that are less prone to distortion-induced fatigue cracking. Specific design alternatives and modern detailing practices, such as avoiding web gaps, providing rigid attachments, using bolted connections, and coping connection plates help minimize secondary stresses in structural details [8]. Therefore, this report focuses exclusively on load-induced fatigue caused by repetitive cyclic stresses.

Estimating the remaining fatigue life of a bridge requires characterizing fatigue damage using either structural analysis or measured strain data. Structural analysis mainly relies on assumptions about fatigue truck loads, distribution, and dynamic effects, while field strain monitoring directly measures the actual stresses experienced by the bridge components [9]. To improve fatigue life prediction based on structural analysis, a structural health monitoring (SHM) based approach has been proposed by researchers in which the finite element (FE) model is updated using ambient vibration measurements, and the remaining life is estimated based on the bridge's current modeled structural condition [10].

3.2 AASHTO FATIGUE PROVISIONS

Fatigue loading is covered in *AASHTO LRFD Bridge Design Specifications* (BDS) 10th edition Article 3.6.1.4 [6]. One HL-93 design truck having the configuration specified in Article 3.6.1.2.2, shown in Figure 1, is used for fatigue loading, but the spacing between the 32 kip axles is fixed at 30 ft. Additionally, the dynamic load allowance from Article 3.6.2 must be used to amplify the fatigue truck loading. This truck loading must be placed anywhere along the bridge longitudinally and transversely to create the maximum stress range at the detail of interest.

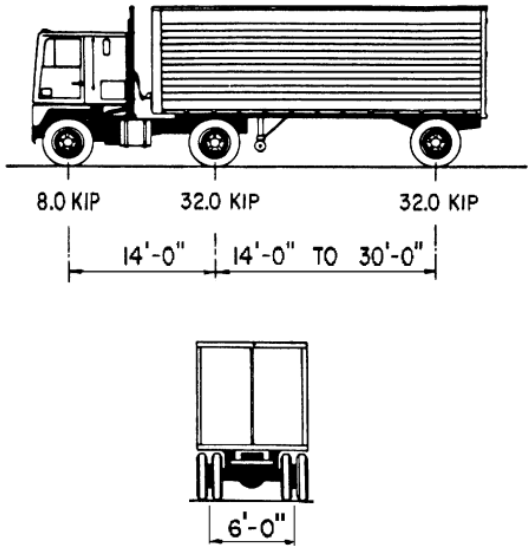

Figure 1. Characteristics of the AASHTO HL-93 design truck [6].

The frequency of fatigue load is represented by single-lane average daily truck traffic ($ADTT_{SL}$), which can be calculated using Equation (1) following.

(1) $ADTT_{SL} = p \times ADTT$

Where:

$ADTT$ = the number of trucks per day in one direction averaged over the design life

p = fraction of traffic in a single lane, as specified in AASHTO LRFD BDS Table 3.6.1.4.2-1

Article 6.6.1 provides the provisions for fatigue considerations, with special requirements for load induced-fatigue assessment provided in Article 6.6.1.2. For fatigue design of steel bridges, live load effects are represented using stress ranges, and these provisions apply only to details subjected to net tensile stresses. AASHTO LRFD BDS adopts a stress-life (*S-N*) curve approach to evaluate the fatigue life of steel bridge components.

Structural steel details are classified into eight categories, known as "detail categories," based on their fatigue resistance. The fatigue resistance of each of these detail categories is represented by a unique lower bound *S-N* curve derived from fatigue test data, corresponding to a 97.5% survival rate, as shown in Figure 2. These detail categories are labeled A, B, B', C, C', D, E, and E', with Category A having the highest fatigue resistance and Category E' having the lowest.

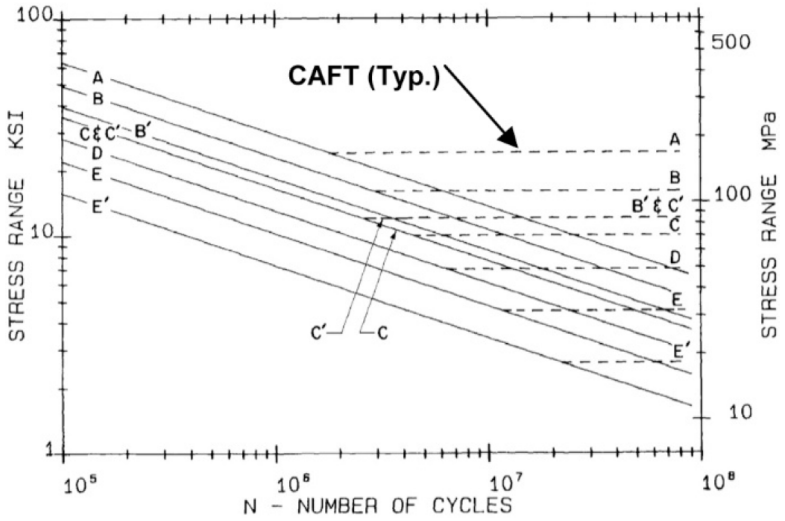

Figure 2. S-N curves for different detail categories [6].

Each S-N curve is composed of two regions, the finite fatigue life region and the infinite fatigue life region. If the stress range is above the constant amplitude fatigue threshold (CAFT), the detail has a finite life, meaning that it is expected to crack after the application of a finite number of cycles. This condition is represented by the sloped line in Figure 2. Similarly, if the stress range is below the CAFT, the detail has an infinite life. In other words, it is predicted to withstand an unlimited number of stress cycles with amplitude less than the CAFT, and fatigue crack initiation and propagation leading to failure will not occur. The horizontal dashed lines in Figure 2 represent the case for infinite life for the detail. Equation (2) describes the infinite fatigue life region for the allowable stress range due to the fatigue truck loading $(\Delta F)_n$ and Equation (3) describes the relationship between $(\Delta F)_n$ and the number of cycles to failure, *N*, in the finite life region [6].

(2) $(\Delta F)_n = (\Delta F)_{TH}$ (for the Fatigue I load combination and infinite life)

(3) $(\Delta F)_n = \left(\frac{A}{N}\right)^{\frac{1}{m}}$ (for the Fatigue II load combination and finite life)

where:

$(\Delta F)_{TH}$ = constant-amplitude fatigue threshold (CAFT) taken from Table 6.6.1.2.3-1 (ksi)

A = constant specific to detail category taken from Table 6.6.1.2.5-1 (ksi^m)

m = fatigue growth constant taken from Table 6.6.1.2.3-1

N = Number of cycles to failure, $(365)(75)n(ADTT)_{SL}$

n = number of stress range cycles per truck passage taken from Table 6.6.1.2.5-1

$(ADTT)_{SL}$ = single-lane ADTT as specified in Article 3.6.1.4.

The constants for each fatigue detail category are presented in Table 1.

Table 1. Fatigue detail category constants from AASHTO LRFD BDS.

Detail Category	Constant, A (ksi^3)	Fatigue Growth Constant, m	CAFT, (ksi)
A	2.50×10^{10}	3	24
B	1.20×10^{10}	3	16
B'	6.10×10^{9}	3	12
C	4.40×10^{9}	3	10
C'	4.40×10^{9}	3	12
D	2.20×10^{9}	3	7
E	1.10×10^{9}	3	4.5
E'	3.90×10^{8}	3	2.6

In fatigue design of bridges, Category C or better is recommended for primary members that are subjected to partial or full tension and are classified as nonredundant steel tension members (NSTMs) or system redundant members (SRMs). However, the code does not directly prohibit the use of fatigue details lower than Category C. For example, some elements of bolted and welded connections for cross-frame and diaphragm members in beam and girder bridges are classified in categories lower than Category C and yet have not experienced any issues related to load induced fatigue damage in field observations [6], [7].

3.3 FATIGUE OF STEEL BOX GIRDERS

Like steel I-girder bridges [11], there are several locations, connections, and geometric features that may be susceptible to load-induced fatigue in steel box girders. Welded attachments such as

transverse web stiffeners, plates welded to girder, utility brackets and support attachments are major fatigue-prone details. Other similar details include diaphragm and cross-frame connections, web to flange welds, deck to girder connection regions, flange and rib splices, cutouts and access holes, internal box girder components.

Due to the bending action induced by traffic loads, the welded connection between the flange and web of girders may experience alternating tensile and compressive stress. Although flange-to-web welded connections are generally considered favorable fatigue details, stress concentrations may cause fatigue damage. So, the fatigue performance of these connections heavily depends on the weld quality, residual stress, and fabrication tolerances [12].

The intersections between transverse and longitudinal web stiffeners are considered prone to fatigue failure. At this intersection, the stress concentration fields of both the stiffeners overlap, making these intersections susceptible to fatigue failure [13]. Steel box girders are fabricated in segments and assembled in field and splices may be necessary depending on the span. These splices need to transfer bending moment, shear and axial forces between connected segments. Under cyclic traffic loads, fatigue cracks may initiate and propagate from the splice plates, bolts, or welds.

Cut-outs present in the diaphragm of steel box and tub girder bridges are also considered fatigue critical details due to high stress concentrations around the cutout boundaries. Finite element modeling suggests that the configuration of cutouts can be optimized for better fatigue performance. Appropriate increase of the radius of cutout and the thickness of diaphragm will increase the fatigue life of the cutout. Among commonly used shape of cutouts in rigid diaphragm, the best shape to prevent fatigue is an arc-straight line [14].

CHAPTER 4 - METHODS

4.1 DATA COLLECTION SYSTEM

4.1.1 BDI System

A Bridge Diagnostics, Inc. (BDI) data acquisition (DAQ) system was selected as the monitoring system given its reliability and flexibility to capture high frequency signals for long-term monitoring. The BDI DAQ system could capture signals from a wide range of sensors, including strain gauges, accelerometers, and weather sensors, and allows synchronized multi-channel acquisition across distributed sensor networks.

For this project, the system was configured with a set of analogous accelerometers to collect the vibration data required for modal identification and model updating. The accelerometers were installed at designated locations to capture the dynamic response of the bridge. The accelerometers had a measurement range of ±5 g, a frequency response of 0-400 Hz, a differential sensitivity of 400 mV/g, and required a 5 V excitation voltage supplied by the data logger's terminal nodes. This frequency range was well suited to capturing the low-frequency dynamic response typical of long-span bridges. The accelerometers were installed at designated locations selected to capture the dominant mode shapes of the structure, as explained in Section 5.1.2.

The core of the monitoring system was a data logger that ran the local acquisition software, collecting and storing synchronized data at a 200 Hz sampling rate, additional details are provided in Section 4.1.2. The data logger is a standalone Windows-based industrial computer with an Intel Core i5-8500T CPU at 2.1 GHz, with 8.0 GB of installed RAM, and a data storage capacity of 1 TB, sufficient to store more than one month of continuous monitoring data before reaching full capacity. The unit measured 240 mm (W) x 225 mm (D) x 79 mm (H) and weighed 3.1 kg. The acquisition software allowed configuration of sampling rate, recording schedules, and supported both continuous recording and event-triggered acquisition. For long-term monitoring, the data logger was housed in a secure, climate-controlled cabinet near the east support of the north arch, protecting the equipment from moisture and unauthorized access, as shown in Figure 3.

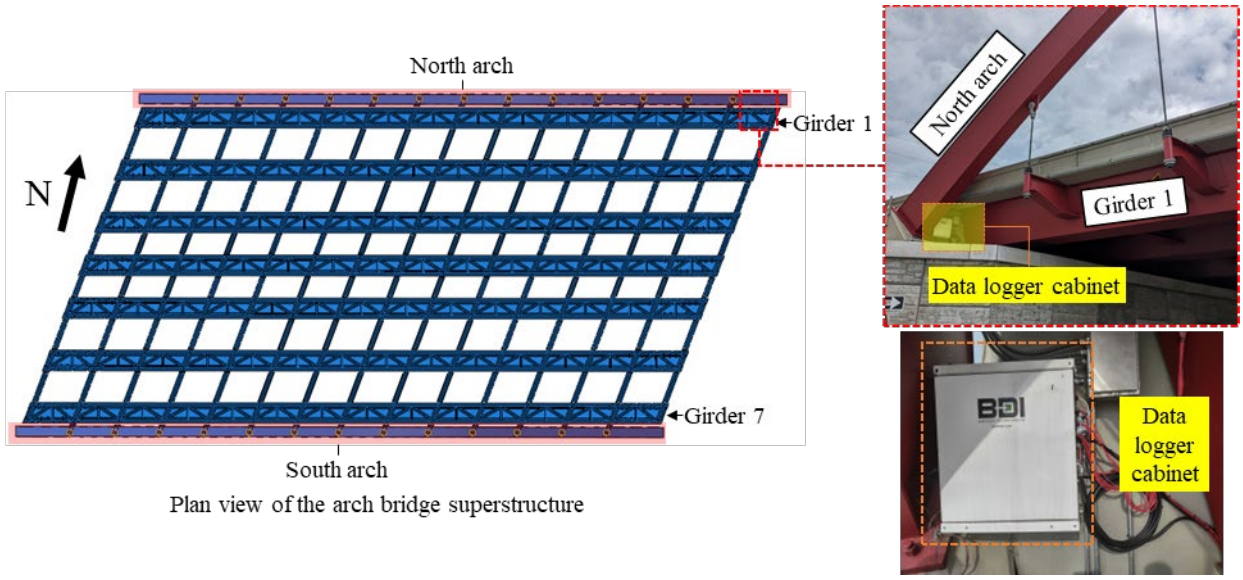

Figure 3. Photos and relative location of data logger cabinet.

The data logger had two Ethernet ports for communication. One connected to 4- and 16-channel terminal nodes, that served as the interface between the data logger and the sensors, converting analog signals from the accelerometers into digital signals. The other Ethernet port provided internet connectivity via a modem located inside the cabinet that was connected to the City of Tuscaloosa network. This port allows the acquisition system to be accessed remotely for data retrieval, system diagnostics, and configuration changes without requiring on-site visits. Figure 4. shows a photo inside the data logger cabinet, along with photos of the 4- and 16-channel terminal nodes and a typical accelerometer installed on the bridge.

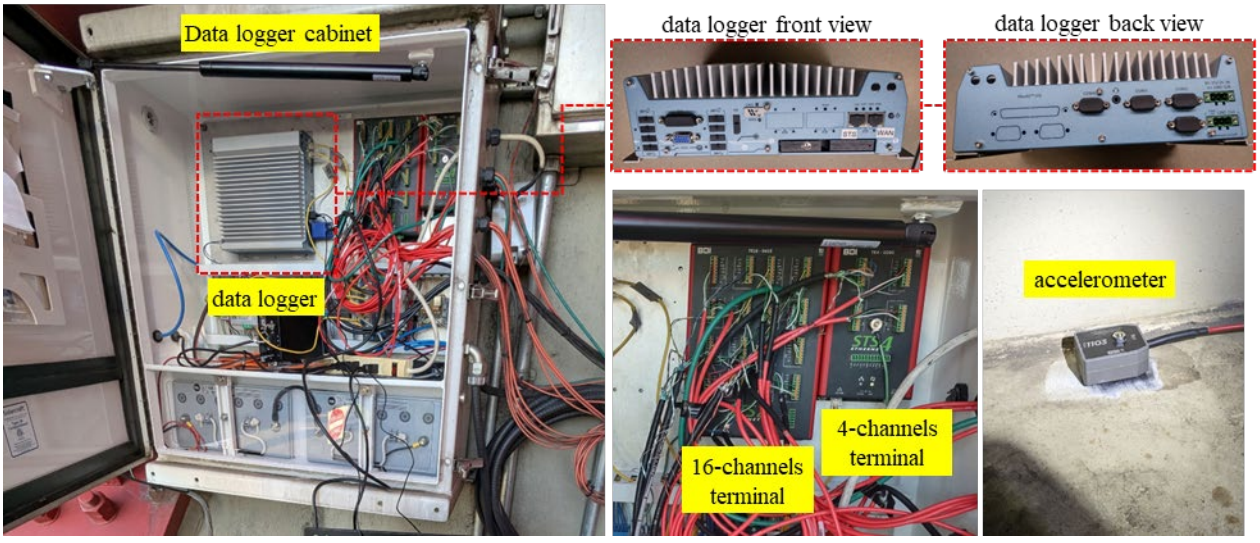

Figure 4. Photos of data logger, 4- and 16-channel terminal nodes, and an accelerometer

4.1.2 Data Collection and Transmission

A reliable data collection and transmission workflow was developed for the long-term monitoring system installed on the I-20/59 McFarland Bridge. The main purpose of this workflow was to collect bridge response data at regular intervals, transfer the recorded files from the field computer to a shared cloud location, and make the data available to the research team through local network storage. This setup reduced the need for frequent field visits and helped ensure that the collected data could be reviewed and processed throughout the monitoring period.

The monitoring system collected time, temperature, and acceleration data from the bridge instrumentation system. These measurements were recorded using the BDI data logger installed at the bridge site, shown in Figure 4. The system was configured to collect 5 minutes of data at a sampling rate of 200 Hz every hour. This collection schedule provided repeated measurements throughout the day while limiting the total amount of data that needed to be stored and transferred. The hourly schedule also provided a practical balance between capturing regular bridge response information and maintaining a manageable data volume for long-term monitoring.

In addition to the regular hourly monitoring schedule, the data collection plan was adjusted during selected high-traffic periods. During the University of Alabama football season, the system was set to collect data continuously over weekends when home football games were expected to increase traffic demand on the bridge. This temporary monitoring mode provided a more complete record of bridge response during periods with higher traffic volume and heavier loading activity. The additional data collected during these weekends captured more diverse excitation conditions, providing a stronger baseline for modal analysis and subsequent model updating.

The data collection process was automated using Windows Task Scheduler and a batch script. At the beginning of each scheduled run, the script launched the local acquisition software on the data logger. The software then recorded data based on the configured test settings and saved the output files locally on the data logger. Although the actual data recording duration was 5 minutes, the scheduled task was given a 30-minute operating window. This longer window was used to allow the software to establish connection with the sensors and confirm proper communication before recording began. Based on system testing, the time required for the software to open and begin recording varied by several minutes. The 30-minute window therefore allowed enough time for the software to start, complete the recording, and close without interrupting the data file creation process.

The scheduled task was also configured to reduce the risk of software conflicts during long-term operation. The task was set to run whether or not the user was actively logged into the computer, and the system was configured to prevent multiple instances of the task from running at the same

time. This was important because overlapping runs could interfere with the acquisition software or create incomplete data files. After each run, log files were created to record the start and stop status of the automated collection process. These logs provided a simple way to confirm that the hourly data collection task had executed as expected.

After the data was recorded, the files were stored locally on the data logger in technical data management streaming (TDMS) format. The TDMS format was used as the direct output format from the acquisition software. The files were organized in date-based folders, which allowed the data to be grouped by collection day. This folder structure was also used by the transmission script when identifying which files needed to be uploaded to the shared project storage location.

A separate automated process was developed to transmit the data collected from the data logger to the shared cloud location. This process was designed to upload the previous day's TDMS files rather than transferring data continuously throughout the day. Uploading one day of data at a time made the transfer process more stable and reduced the chance of large upload sessions interfering with the hourly data collection task. The script was also configured to copy only new or modified TDMS files, which helped avoid duplicate transfers and reduced unnecessary upload time.

The cloud upload task was scheduled to run overnight, with a primary upload at 12:35 AM and a backup upload at 3:35 AM. These times were selected because traffic volume was expected to be low during these hours, minimizing the risk that any interference with the data acquisition process would result in the loss of meaningful data. During testing, it was observed that active cloud synchronization could slow down the data logger. For this reason, the upload was scheduled outside the main data collection period as much as possible. The backup upload time was added to improve reliability in case the first upload did not run successfully, such as during a temporary power or system interruption.

The transmission script included a verification step after the files were copied to the cloud. The script compared the number of TDMS files and the total file size between the local source folder and the cloud destination folder. If the file count and total size matched, the upload was considered successful. If the verification did not pass, the log files could be reviewed to identify the issue and determine whether the upload needed to be repeated. This verification step was included to reduce the chance of missing or incomplete data transfers.

In addition to the cloud upload process, a network-attached storage (NAS) system was fully set up to retrieve the bridge data from the shared cloud folder and store it locally on the University of Alabama network. This provided the research team with a second access point for the monitoring data and allowed the files to be available offline for later processing and review. The NAS setup also supported better organization of the long-term dataset by keeping a local copy of the files collected from the bridge.

Overall, the implemented workflow provided an automated path from field data collection to shared data access. The DAQ system collected time, temperature, and acceleration data from the bridge every hour, the TDMS files were stored locally on the field computer, the previous day's files were uploaded to the cloud during the overnight period, and the NAS system retrieved the uploaded files for local access by the research team. This workflow improved the reliability and accessibility of the monitoring data while reducing the need for manual file transfer from the bridge site.

4.2 VIBRATION MODAL ANALYSIS

The objective of vibration modal analysis is to capture the dynamic response of the real structure, specifically its natural frequencies and mode shapes. This measured response was then used to update a numerical model of the structure, providing an experimentally validated basis for the fatigue life predictions.

Given the size and importance of the bridge, conventional dynamic testing methods such as hammer impact tests are impractical, since these methods struggle to introduce sufficient excitation energy across the full frequency range of interest for a structure of this scale. In this project, operational modal analysis (OMA) [15] was conducted instead, using ambient vibration measurements obtained during normal traffic operation over an extended monitoring period.

The natural excitation technique (NExT) combined with the eigensystem realization algorithm (ERA) [16] was used to extract the modal parameters, including natural frequencies and mode shapes from the recorded vibration signals. NExT converts the ambient vibration response into a set of impulse response-like functions by computing cross-correlations between accelerometer channels, under the assumption that the input excitation approximates a stationary random process. These correlation functions are then treated as free-decay responses and passed to ERA, which identifies a state-space realization of the system from which the modal parameters are extracted.

ERA constructs this realization by arranging the free-decay response data into a Hankel matrix [16] and calculating its singular value decomposition, from which a minimal state-space realization can be constructed to derive modal frequencies and mode shapes. Because the resulting realization depends on the chosen Hankel matrix dimensions, ERA was repeated over a range of dimensions, along with a range of reference channels, to produce multiple realizations for identifying consistent, physical modes. Since this identification process can produce both physical and fictitious modes, several checks were used to isolate the modes that represent real structural behavior.

ERA was run repeatedly across different reference channels and data window sizes, generating a broad set of candidate modal estimates. A stabilization diagram was used to isolate physical

modes from this population, retaining only modes that recurred across a sufficient percentage of the realizations, and these stable modes were further grouped by spatial consistency to extract a representative natural frequency and mode shape for each mode of interest. The stabilization diagram was also overlaid on the measured vibration spectrum, providing a cross-check that the retained modes align with real structural peaks, while inconsistent or spurious results were discarded. Figure 5. illustrates this process, showing the stabilization diagram overlaid on the normalized power spectral density (PSD) of the measured channels, where the red vertical lines mark frequencies at which stable modes are identified across a sufficient number of realizations. Further, these red vertical lines coincide with peak locations on the PSD.

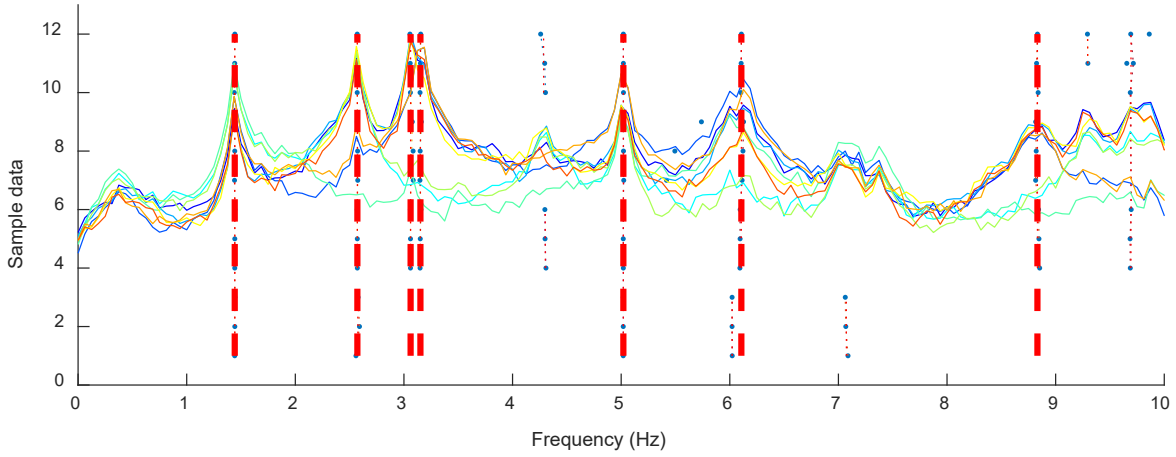

Figure 5. Stabilization diagram overlapped with the normalized PSD. Red vertical lines indicate stable, physical modes identified across a set of candidates.

The resulting experimental modal parameters were compared against the numerical modal parameters obtained from the finite element model in ABAQUS. This comparison used the modal assurance criterion (MAC) to quantify the correlation between experimental and numerical mode shapes, along with the percent difference in natural frequencies for each corresponding mode pair. Discrepancies between the two sets of modal parameters guided the model updating process, in which a select number of structural parameters are adjusted to improve agreement between the numerical model and the measured dynamic response.

CHAPTER 5 - I-20/59 AND MCFARLAND BRIDGE

5.1 BRIDGE OVERVIEW

5.1.1 General Overview

The bridge was designed in accordance with the *AASHTO LRFD Bridge Design Specifications, 6th Edition*. According to Section 3.6.1.4.2 of *AASHTO LRFD BDS*, single-lane average daily truck traffic, $ADTT_{SL}$, generally represents the frequency of the fatigue load. For this bridge, the projected average daily traffic (*ADT*) for the year 2037 is 98,323 vehicles per day. For the estimation of $ADTT_{SL}$, 60% of *ADT* traffic is assumed to travel in one direction, and 34% of the *ADT* is assumed to be truck traffic. For a three-lane roadway, a lane distribution factor of 0.8 is applied which represents the proportion of traffic in a single lane. Accordingly, the $ADTT_{SL}$ for the year 2037 was calculated by the bridge designers to be 16,046 trucks per day.

Traffic volumes in Tuscaloosa exhibit strong seasonal fluctuations associated with the University of Alabama home football games. The University of Alabama hosts six to seven home football games each fall. During home football games, Tuscaloosa experiences an influx of more than 100,000 fans, resulting in significantly increased traffic volumes [17]. Interstate 20/59 (I-20/59) serves as the primary gateway for fans travelling to Tuscaloosa, resulting in a significant increase in traffic volume along this route during game days. Transportation networks must accommodate not only the passenger vehicles but also buses, trucks, service vehicles and other support vehicles for gameday operations.

As fatigue damage is mainly initiated by truck traffic rather than the total increase in traffic volume, the effect of seasonal variation in traffic due to home football games on fatigue damage remains uncertain. The proportional contribution of seasonal traffic increase to truck traffic is currently undetermined. It is likely small, as most visitors to football games are expected to travel using passenger cars. Hence, the impact of seasonal traffic variations on the fatigue life of the bridge components cannot be directly determined without information on truck traffic variation.

The I-20/59 McFarland bridge is a single-span steel tied-arch bridge with a total length of about 256 ft 10.25 in and a total width of about 129 ft 5 in. The bridge superstructure consists of seven longitudinal steel box plate girders, fifteen transverse floor beams, and two exterior steel arch ribs. The bridge abutments are skewed, with a skew angle of 69°24′59″. Figure 6 presents the framing plan of the bridge superstructure, including the girder layout, floor beam arrangement, and lateral bracing system.

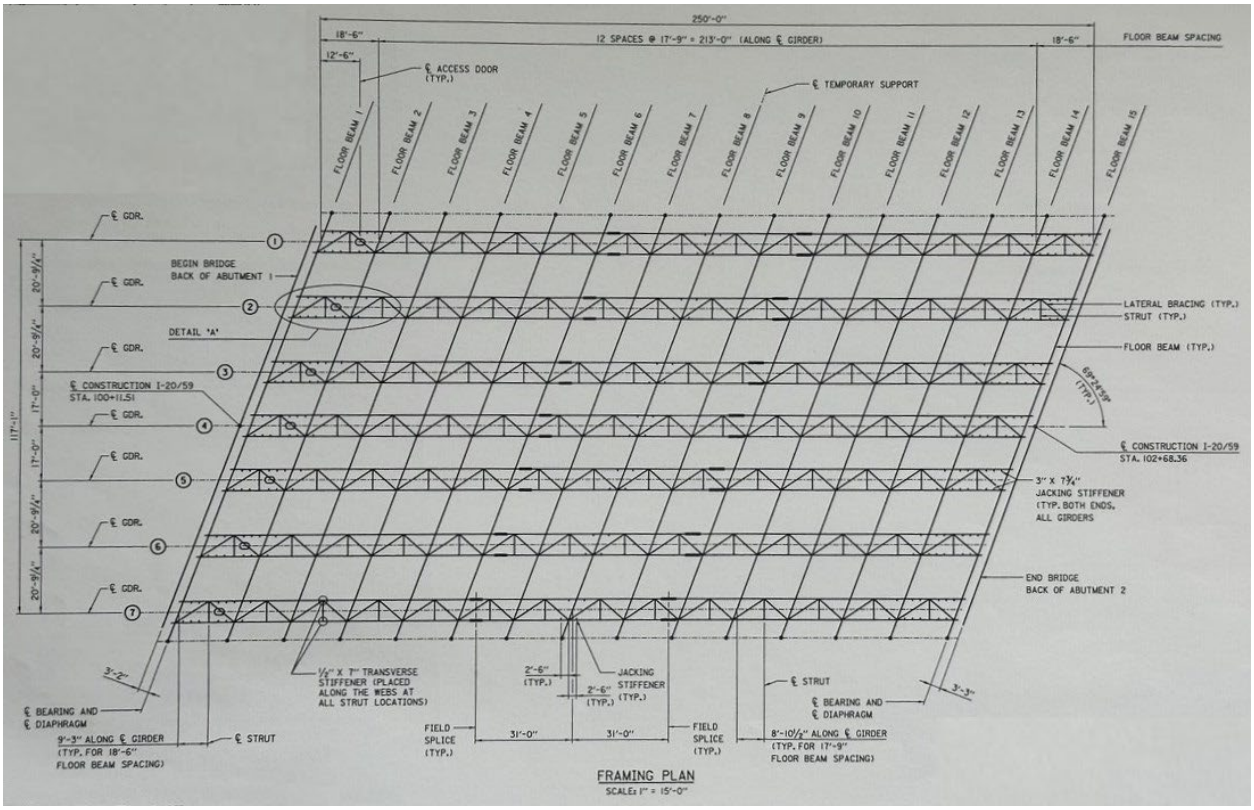

Figure 6. Framing plan of the arch bridge superstructure.

The seven longitudinal girders are spaced 20 ft 9.25 in center-to-center, except between girders 3 and 4 and girders 4 and 5, where the spacing is reduced to 17 ft. Fifteen transverse floor beams are provided between the girders to transfer deck loads and improve transverse stiffness. The spacing between adjacent floor beams is generally 17 ft 9 in. Unlike conventional steel I-girder bridges that utilize intermediate cross-frames, the I-20/59 McFarland bridge employs floor beams as the primary transverse framing system.

Figure 7 illustrates the elevation view of the tied-arch rib and hanger system from the shop drawings. The bridge utilizes a parabolic tied-arch configuration with vertically oriented hanger cables connecting the arch ribs to the transverse floor beams. A total of 26 hangers are used in the bridge, with 13 hangers positioned along each side. The figure also identifies the locations of the hanger connections and the field splices along the arch ribs.

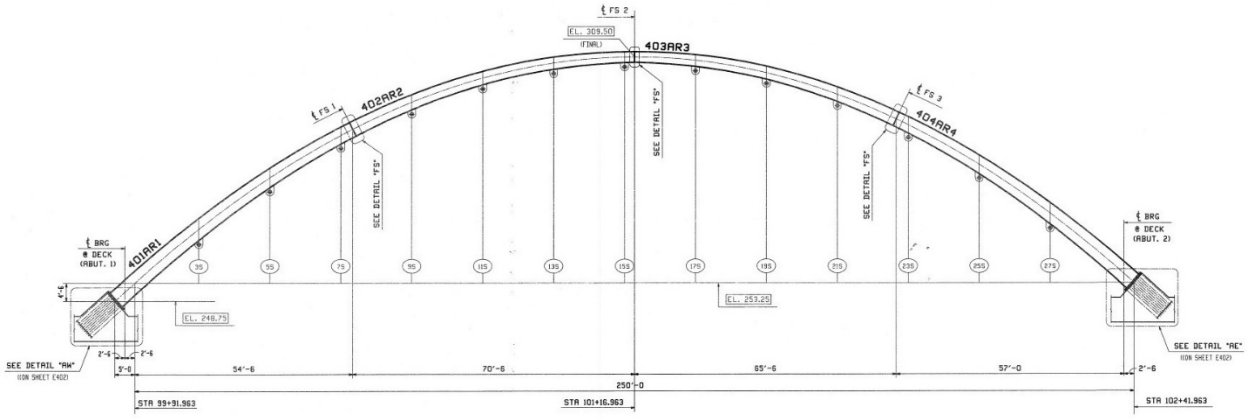

Figure 7. Elevation view of the arch rib and hanger system.

The longitudinal box girders are fabricated as steel plate girders with sloped webs, internal stiffeners, and longitudinal lateral bracing members. Figure 8 presents the typical transverse section of the bridge deck, while Figure 9 illustrates a typical girder section. The girder webs have a depth of 6 ft and a thickness of 0.5 in. The top flange consists of two 18-in-wide plates, each with a thickness of 1 in, whereas the bottom flange is 4 ft wide and 2 in thick. The flange plates are 0.25 in thicker near the midspan of the girders. Elliptical openings with outside dimensions of 3 ft by 2 ft are provided within the internal stiffeners inside the box girders to accommodate utilities and to provide inspection access to the interior of the girders.

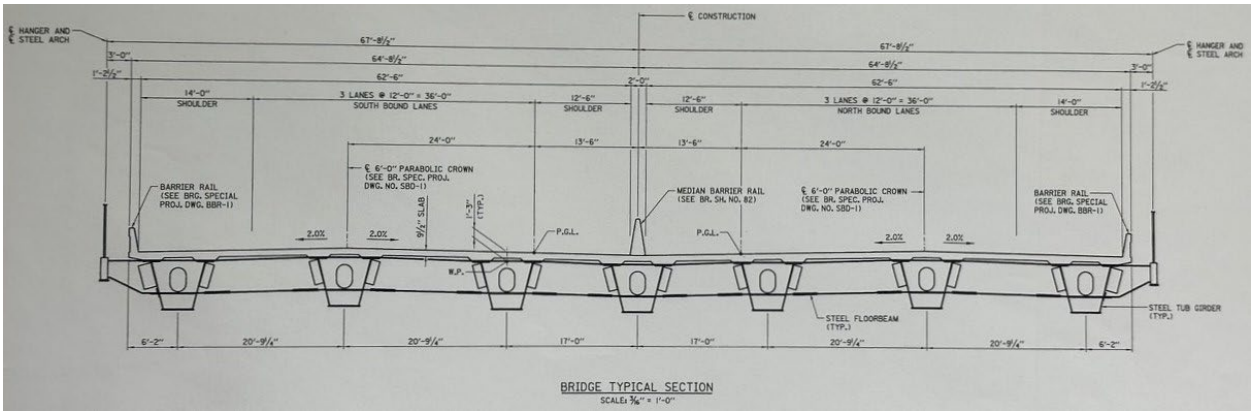

Figure 8. Typical cross section of the bridge illustrating the deck width, girder arrangement, and transverse geometry.

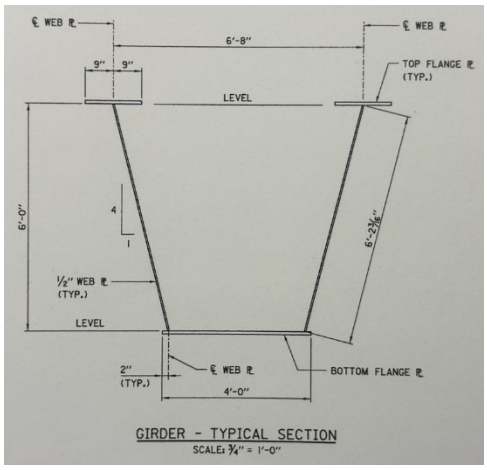

Figure 9. Typical girder cross-sectional details showing the geometry and dimensions of the steel box girder components.

The arch ribs consist of closed steel box sections with internal stiffeners, as shown in Figure 10. The arch rib section has a depth of 4 ft 10 in at the base and 2 ft 11 in at the crown, a top flange width of 4 ft 6.5 in at the base and 3 ft 7 in at the crown, and a bottom flange width of 2 ft 3 in. The top and bottom flanges have a thickness of 1.5 in, while the webs have a thickness of 1.25 in. The bridge deck consists of a reinforced-concrete slab with an average thickness of 9.5 in supported by the steel floor beams.

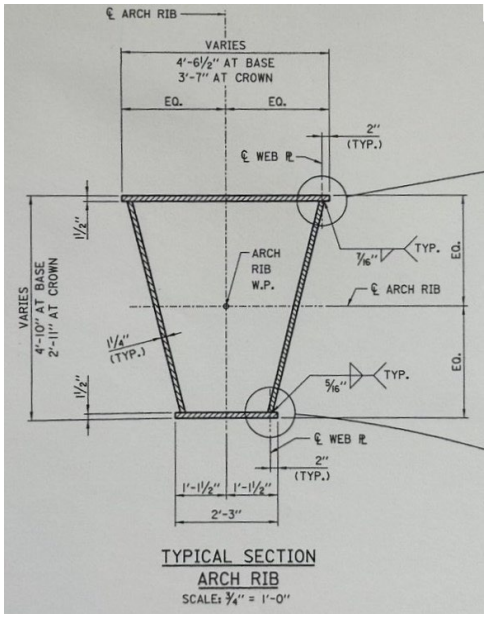

Figure 10. Arch rib cross-sectional details showing the geometry and dimensions of the steel box section.

5.1.2 Instrumentation Plan

The installation of the DAQ system and sensors took place in multiple phases, including during construction of the bridge and after its completion, with BDI serving as a consultant throughout the installation process. In total, 15 accelerometers were installed on the girders and arches of the bridge at critical locations to capture the global dynamic behavior of the structure. The accelerometers installed on the girders consisted of nine uniaxial accelerometers oriented to measure vertical vibration. Six accelerometers were installed on the arches, including four uniaxial and two biaxial accelerometers. The two biaxial accelerometers were installed at the mid-span location on the arches to capture vertical and lateral (wind-induced) vibration, while the remaining four accelerometers were installed with the measuring direction perpendicular to the bottom surface of the arches near the hanger cables connected to floor beams 5 and 11. This number of sensors was selected to provide sufficient spatial resolution to characterize the principal vibration modes of the bridge. Figure 11 presents the instrumentation layout for the project, including the relative location of the sensors, and photos documenting their physical location.

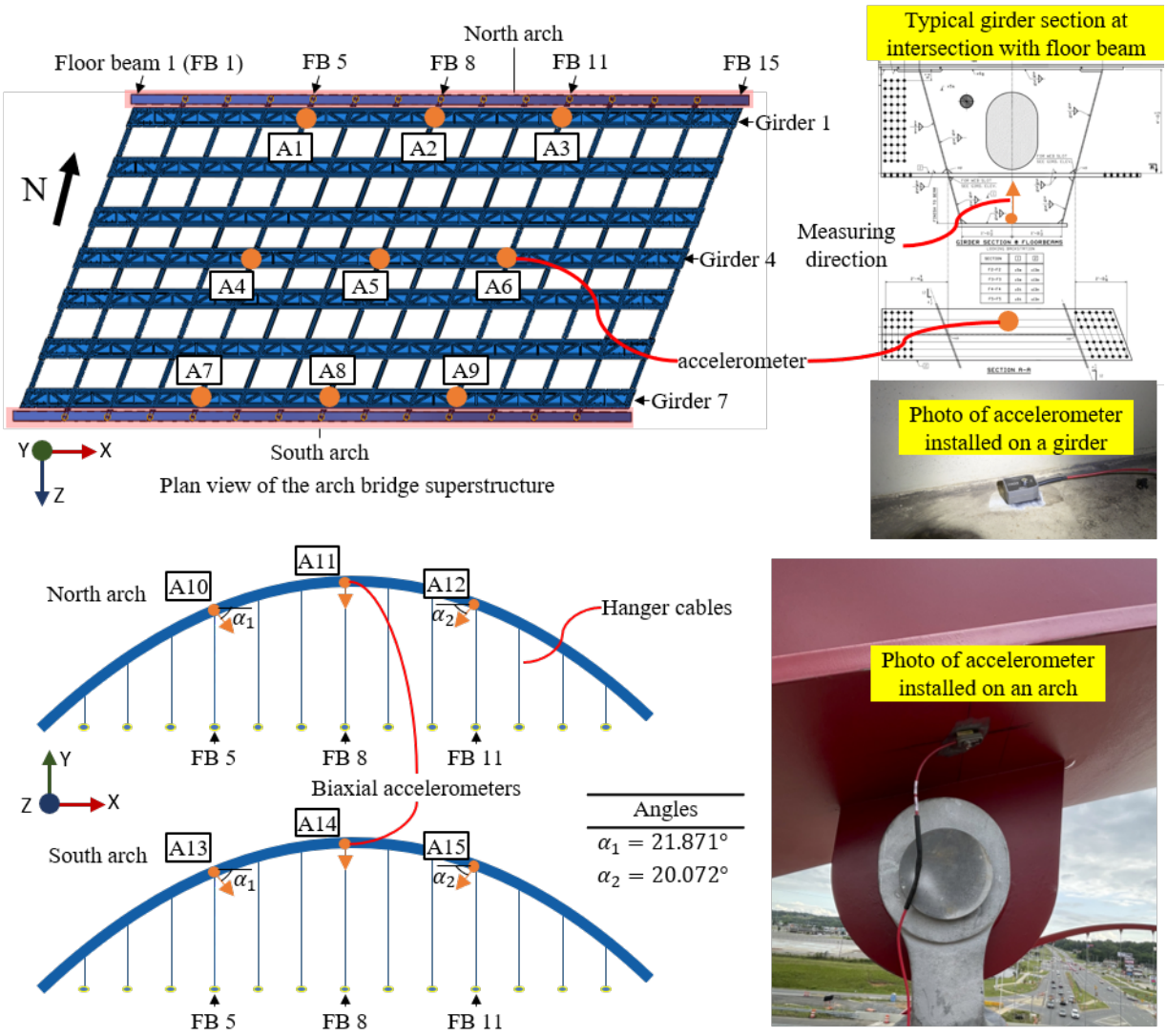

Figure 11. Instrumentation layout and photos of accelerometer installed on a girder and an arch.

As shown in Figure 11, accelerometers were installed at the mid-span (near floor beam 8) and near quarter-span (near floor beams 5 and 11) locations on the girders and arches to capture the principal vertical and lateral vibration modes. This arrangement was selected because the mid-span and quarter-span locations corresponded to locations of high excitation for the first several vertical bending modes, where modal amplitudes were largest and therefore most reliably measured. For the girders, the sensors were labeled A1 through A9, distributed in sets of three per instrumented girder, A1-A3 were located on girder 1, A4-A6 were located on girder 4, and A7-A9 were located on girder 7. For the arches, the naming convention continued with sensors labeled A10 through A15 distributed on the arches, where A10-A12 were located on the north arch, and A13-A15 were located on the south arch. Each accelerometer was mounted on a mounting tab fixed to the structure via adhesive, and sensor cables were routed inside the girders,

protecting them from environmental exposure, or along the hanger cables. Table 2 summarizes the entire monitoring layout, indicating the measuring direction of each sensor, the structural member where the sensor was installed, and the reference floor beam closest to the sensor.

Table 2. Summary of installed accelerometers with measurement direction and location.

Accelerometer	Measurement direction	Installed on	Intersecting floor beam
A1	Y	Girder 1	5
A2	Y	Girder 1	8
A3	Y	Girder 1	11
A4	Y	Girder 4	5
A5	Y	Girder 4	8
A6	Y	Girder 4	11
A7	Y	Girder 7	5
A8	Y	Girder 7	8
A9	Y	Girder 7	11
A10	-Y, X	North arch	5
A11	-Y, Z	North arch	8
A12	-Y, -X	North arch	11
A13	-Y, X	South arch	5
A14	-Y, -Z	South arch	8
A15	-Y, -X	South arch	11

Furthermore, as explained in Section 4.1.2, the system operated as a long-term monitoring system, collecting data for five minutes every hour at a sampling rate of 200 Hz. This monitoring schedule was adopted to manage the data storage limitations of the data logger over an extended monitoring period, while five-minute recordings provide a representative sample of the ambient vibration response for reliable modal identification, as mentioned in Section 4.1.1. The sampling rate of 200 Hz was well above the Nyquist requirement for the frequency range of interest, since the fundamental modes of the bridge were expected to occur below 20 Hz.

5.2 DATA

5.2.1 Accelerometer Data

Accelerometer data was collected over an intermittent period of five months from October 2025 to February 2026. During this period, data collection followed the schedule described in Section 4.1.2, supplemented with continuous data collection during weekends with heavy traffic expected, e.g. the weekends of home football games. Figure 12 shows the days when data was collected (marked in green) during the five-month monitoring period. Each day produced 24 records, resulting in over 2,000 acceleration records during the monitoring period.

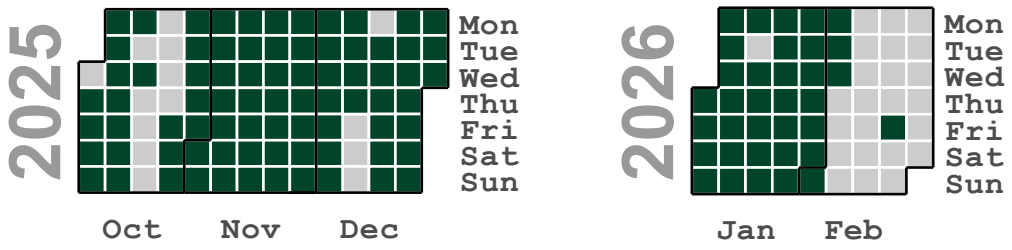

Figure 12. Days when data was collected (marked in green) from October 2025 to February 2026.

Figure 13 presents a typical five-minute recording captured by the accelerometers installed on the girders (A1-A9) on October 05, 2025, from 7:01 PM to 7:06 PM. This time history captured the ambient vibration induced by traffic passing through the bridge. The acceleration amplitude typically fell within ±0.05 g across all channels. For these nine sensors, no signal clipping, saturation, or dropout was observed on any channel, indicating consistent instrumentation performance. Several bursts of elevated amplitude were visible in all channels simultaneously, corresponding to vehicles crossing the bridge, which confirm that the sensor network captures a common structural response.

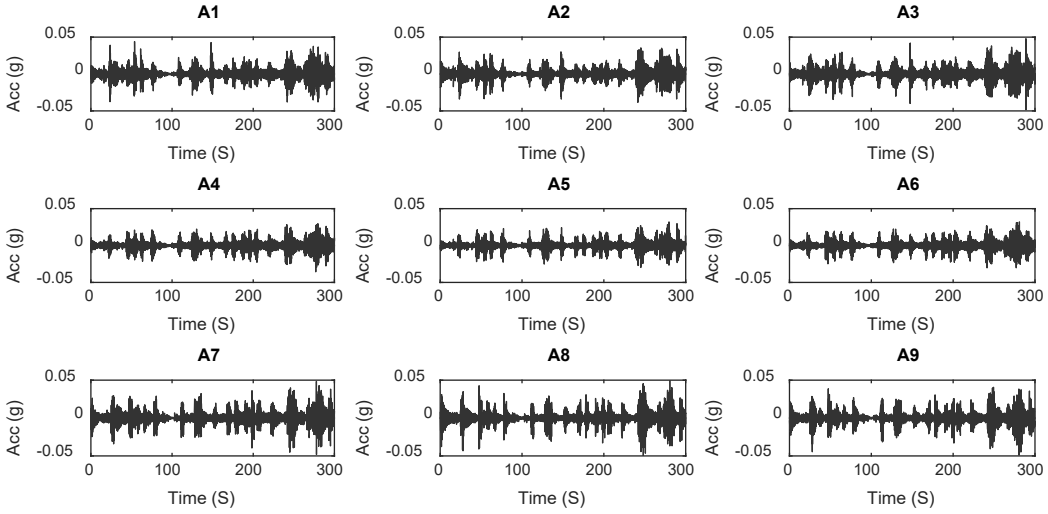

Figure 13. Typical five minute vibration record from sensors installed on the girders.

Figure 14 presents the time history captured by the accelerometers installed on the arches for the same record shown in Figure 13, on October 05, 2025, from 7:01 PM to 7:06 PM. These records indicate that only two of the eight arch channels (A10 and A13) captured the dynamic response of the bridge, displaying similar pattern observed by the accelerometers on the girders in Figure 13. Meanwhile, accelerometers A11(Y), A14(Y), A15, A11(Z), A14(Z) show a flat time history with no discernable ambient vibration, indicating that these channels failed to capture a valid

structural response and were likely non-functional during this monitoring period. Given the uncertainty associated with the data captured by the accelerometers installed on the arches, these sensors were not included in the vibration modal analysis.

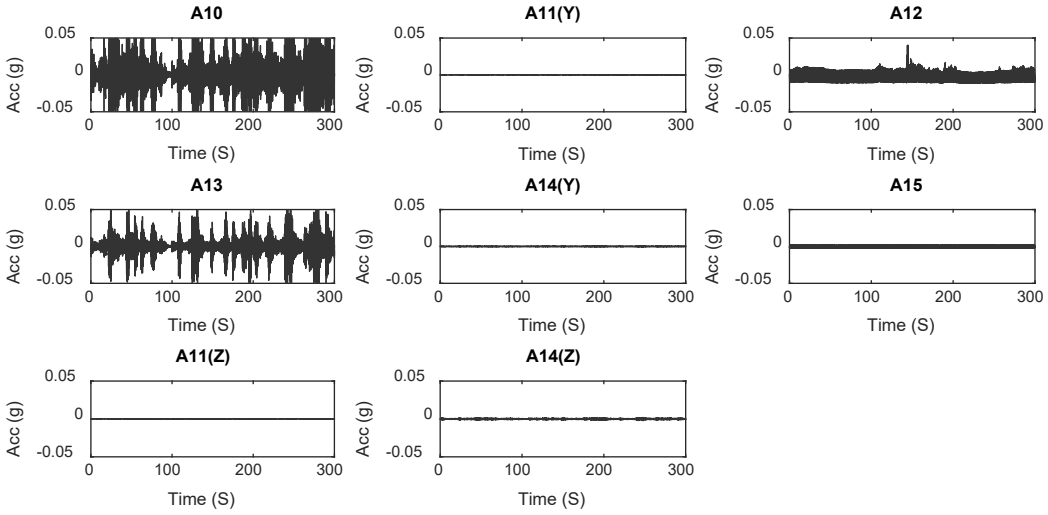

Figure 14. Typical five minute vibration record from sensors installed on the arches.

5.2.2 Vibration Modal Analysis

To perform finite element model updating, the modal parameters (i.e., natural frequencies and mode shapes) of the real structure were identified using experimental data. This analysis considers only the nine accelerometers installed on the girders and therefore captures only the vertical vibration modes of the girders. All collected records were used to independently estimate the bridge's modal parameters using the NExT-ERA technique introduced in Section 4.2.

Since each record produced its own set of identified modes, these individual estimates were aggregated across all records and sorted by frequency to reveal the overall distribution of natural frequencies observed throughout the monitoring period. Because the same physical mode can be identified repeatedly across different records, with slight variation in estimated frequency for each record, clustering was used to group these repeated estimates together. Frequencies that fell within a narrow band of each other were grouped into the same frequency cluster, forming a set of candidate mode groups spanning the full frequency range of interest, as illustrated in Figure 15.

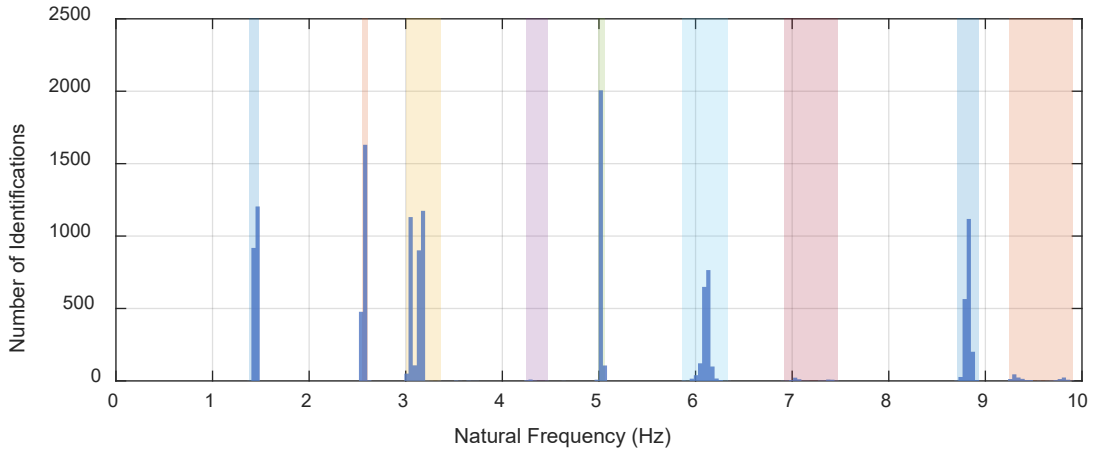

Figure 15. Distribution of identified natural frequencies with clustered (shadowed) regions

Within each frequency cluster, mode shape correlation is used to further separate estimates that share a similar frequency but correspond to physically distinct modes. The MAC is calculated between all mode shapes from the same cluster, and similar mode shapes (MAC>0.8) are grouped into the same sub-cluster. From each sub-cluster, a single representative natural frequency and mode shape are selected, and the sub-cluster containing the largest number of grouped estimates is retained as the most consistently identified mode for that frequency range. This process yields a final set of representative modal parameters for the bridge, each supported by a large number of independent identifications across the monitoring period.

Figure 16 displays the first three identified mode shapes of the bridge, corresponding to natural frequencies of 1.45 Hz, 2.55 Hz, and 3.06 Hz. Modes 1 and 2 correspond to single- and double-curvature vertical mode shapes, while the third mode shape corresponds to a torsional mode.

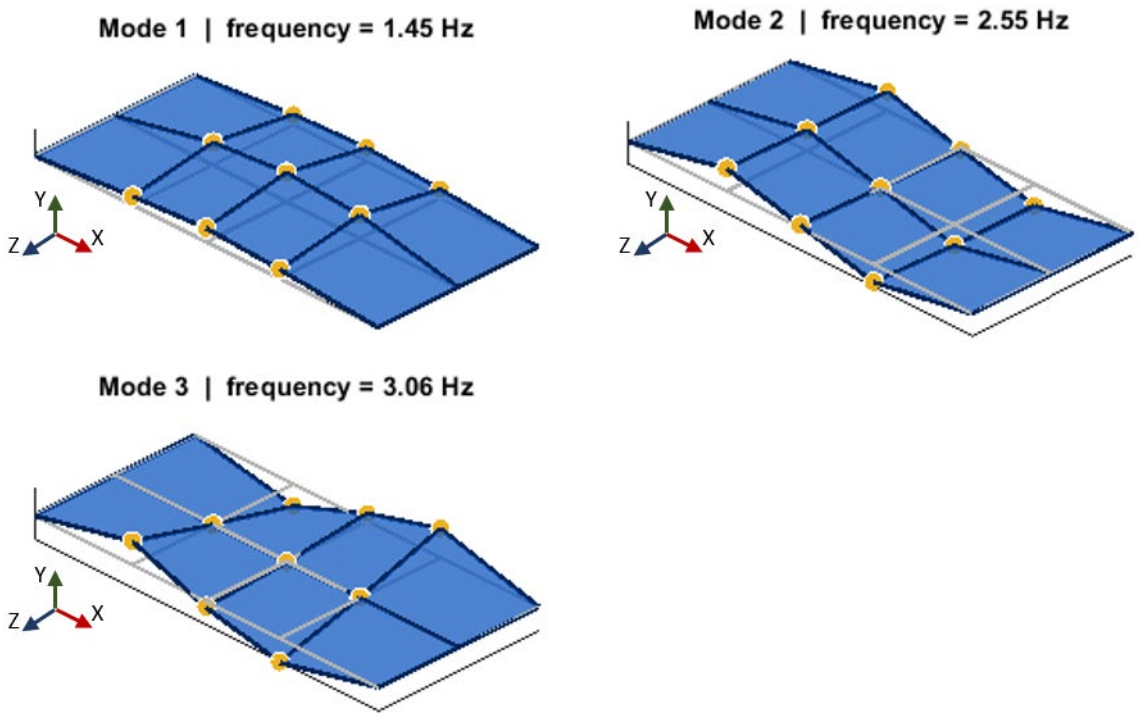

Figure 16. The first three modes identified from modal analysis of the experimental data.

CHAPTER 6 - FINITE ELEMENT MODELING FRAMEWORK

6.1 OVERVIEW

The finite element method (FEM) is a numerical technique widely used in engineering to evaluate the behavior of complex structures under various loading conditions. The method is based on the principles of continuum mechanics, in which a continuous structure is discretized into a finite number of interconnected elements. These elements are interconnected at nodes to form a mesh representing the physical structure. The structural response is obtained by solving a system of equations that accounts for the model geometry, material properties, applied loads, and boundary conditions. The primary solution variables are the nodal displacements, from which stresses, strains, internal forces, and other response quantities can be determined.

Finite element simulations for this project were performed using the commercial software ABAQUS/CAE 2024 [18]. This software is widely used in both research and engineering practice for the analysis of linear and nonlinear structural systems. It provides a comprehensive environment for creating geometric models, assigning material properties, defining interactions, applying loads, and implementing boundary conditions. A detailed three-dimensional finite element model of the I-20/59 McFarland Bridge was developed based on the bridge design and shop drawings obtained from ALDOT. The design drawings and shop drawings are prepared by AECOM and Hirschfeld Industries, respectively. All geometric dimensions, structural details, and material properties incorporated into the model were obtained directly from these drawings.

The finite element model developed in this project was used to investigate the structural behavior and dynamic characteristics of the bridge. In addition, the model was calibrated using experimentally identified modal properties obtained from field acceleration measurements to improve the agreement between the numerical predictions and the measured bridge response, as described in Section 5.2.2. The updated model was subsequently used for the analyses presented in CHAPTER 7 - .

The following sections describe the bridge geometry, material properties, finite element discretization, boundary conditions, loading configurations, and modeling assumptions adopted in the numerical analyses. The procedures used to develop, calibrate, and post-process the finite element model are also presented.

6.2 GEOMETRY

The finite element model of the I-20/59 McFarland Bridge was developed directly from the design drawings and shop drawings to accurately represent the as-designed geometry and structural configuration. A detailed description of the bridge geometry is provided in Section 5.1.1. The bridge is a single-span steel tied-arch structure consisting of seven longitudinal steel box girders, fifteen transverse floor beams, two steel arch ribs, and twenty-six vertical hanger

cables. The geometric dimensions, member configurations, and connection details incorporated into the finite element model are consistent with the design and shop drawings.

To reduce computational effort, the reinforcing bars within the concrete deck were not modeled. Likewise, shear studs, bolt assemblies, and bolt holes were omitted, and the connections between structural components were represented using tie constraints. In contrast, the upper and lower hanger connection assemblies were modeled using shell elements. Figure 17 illustrates the complete finite element model of the bridge.

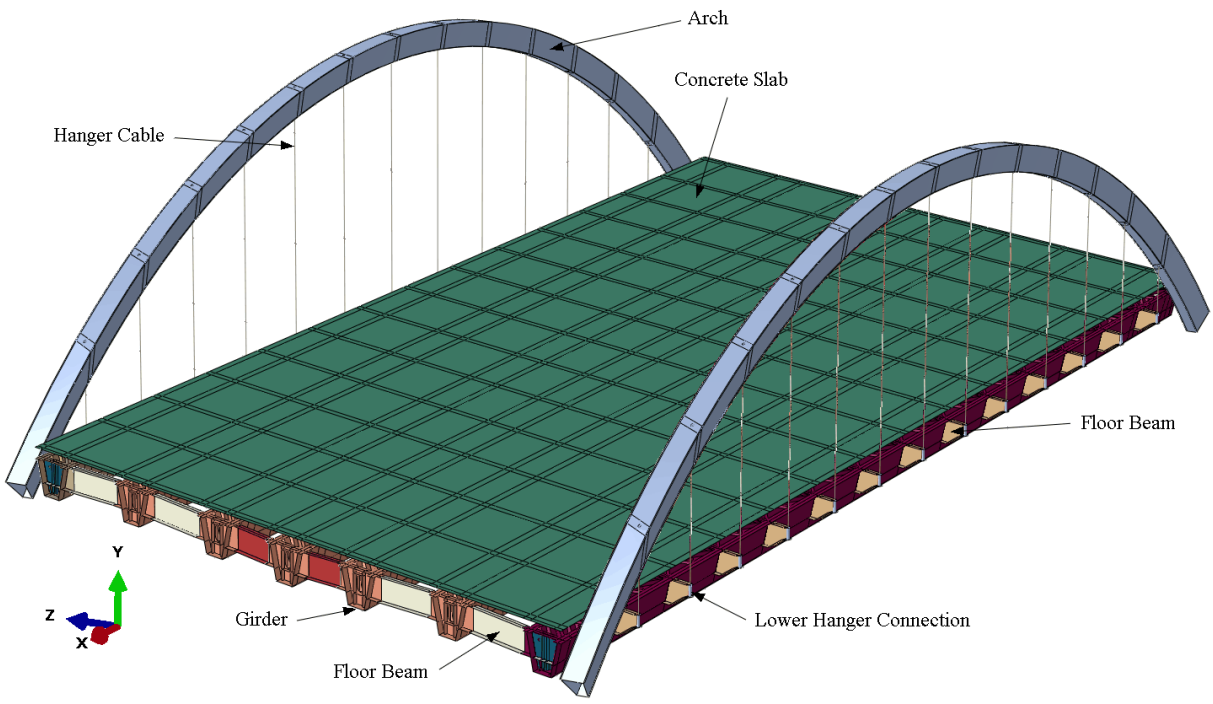

Figure 17. Complete finite-element model of the tied-arch bridge.

6.3 MATERIAL PROPERTIES

In Abaqus, material behavior is defined independently of the model geometry, allowing material properties to be assigned consistently. In this project, linear elastic material models were adopted for both the structural steel components and the concrete deck. The material definition included mass density (ρ), modulus of elasticity (E), and Poisson's ratio (v). The material properties assigned to the structural steel (ASTM A709 Grade 50) and the concrete deck are summarized in Table 3. These properties were obtained from the bridge design drawings and are consistent with the inch-pound-second (IPS) unit system adopted for the finite element model.

Table 3. Material properties used in the finite element model.

Material	Mass Density (slugs/in³)	Elastic Modulus (psi)	Poisson's Ratio
Structural steel	0.0007345	29,000,000	0.26
Normal-weight concrete	0.000224652	3,605,000	0.2

Nonlinear material behavior was not considered in the analysis for this project. Eigenvalue analysis was performed to evaluate the dynamic characteristics of the bridge, including its natural frequencies and mode shapes. Linear elastic material models are sufficient because eigenvalue extraction is based on the initial elastic stiffness and mass properties of the structure, and the stresses induced by the live load analysis do not exceed the elastic limit of the structural steel or concrete deck. Accordingly, the inclusion of plasticity or other nonlinear material effects would not affect the calculated modal properties or the live load response but would increase the computational effort.

6.4 BOUNDARY CONDITIONS

The I-20/59 McFarland Bridge is a skewed, simply supported structure supported by bearings at the two abutments, as shown in Figure 18. Each abutment contains seven bearings, one for each longitudinal girder, positioned at different elevations to accommodate the bridge geometry.

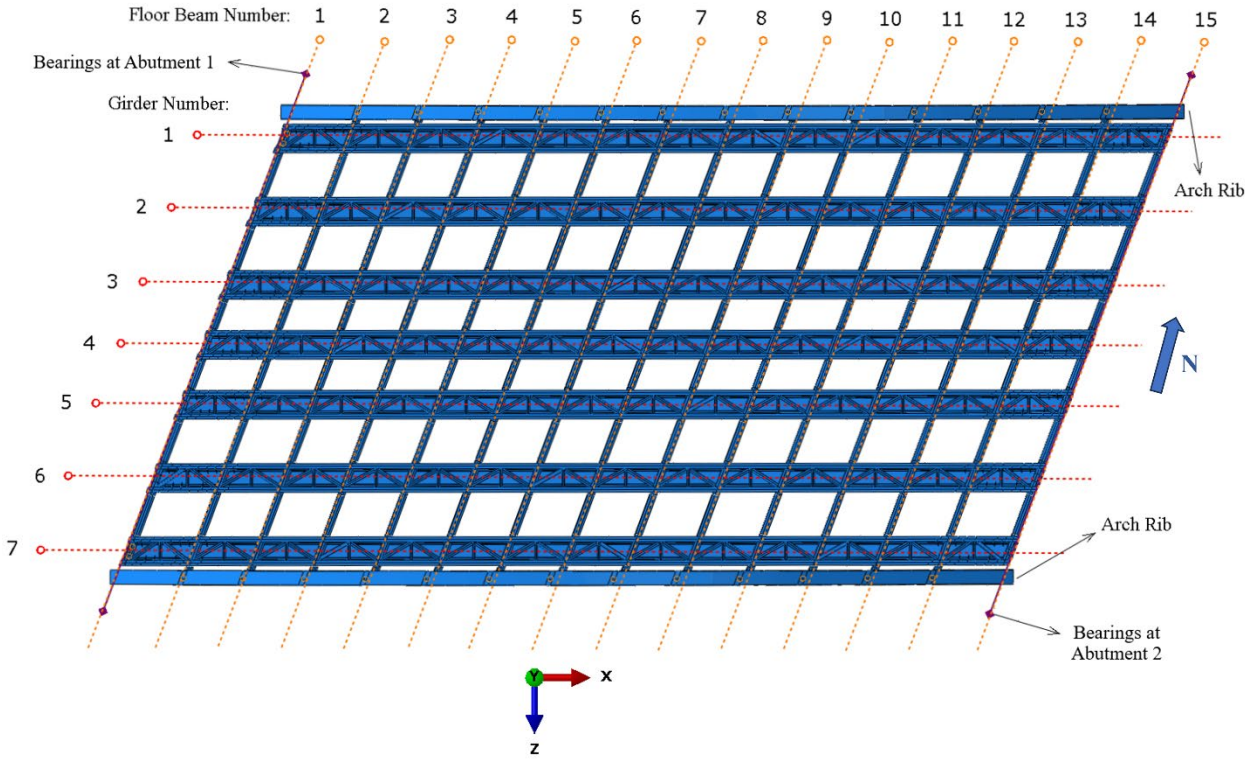

Figure 18. Layout of the I-20/59 bridge showing abutments, bearings, longitudinal girders, transverse floor beams, and arch ribs.

Four types of boundary conditions were used at the girder ends: specialized roller bearings that restrain lateral displacement and torsional rotation (R), fixed bearings permitting rotational freedom (F), non-guided expansion bearings (NE), and longitudinally guided elastomeric bearings (GEL). Figure 19 presents the bearing layout adopted for the bridge model, and Figure 20 presents photographs of the specialized roller (R) and non-guided expansion (NE) bearing supports.

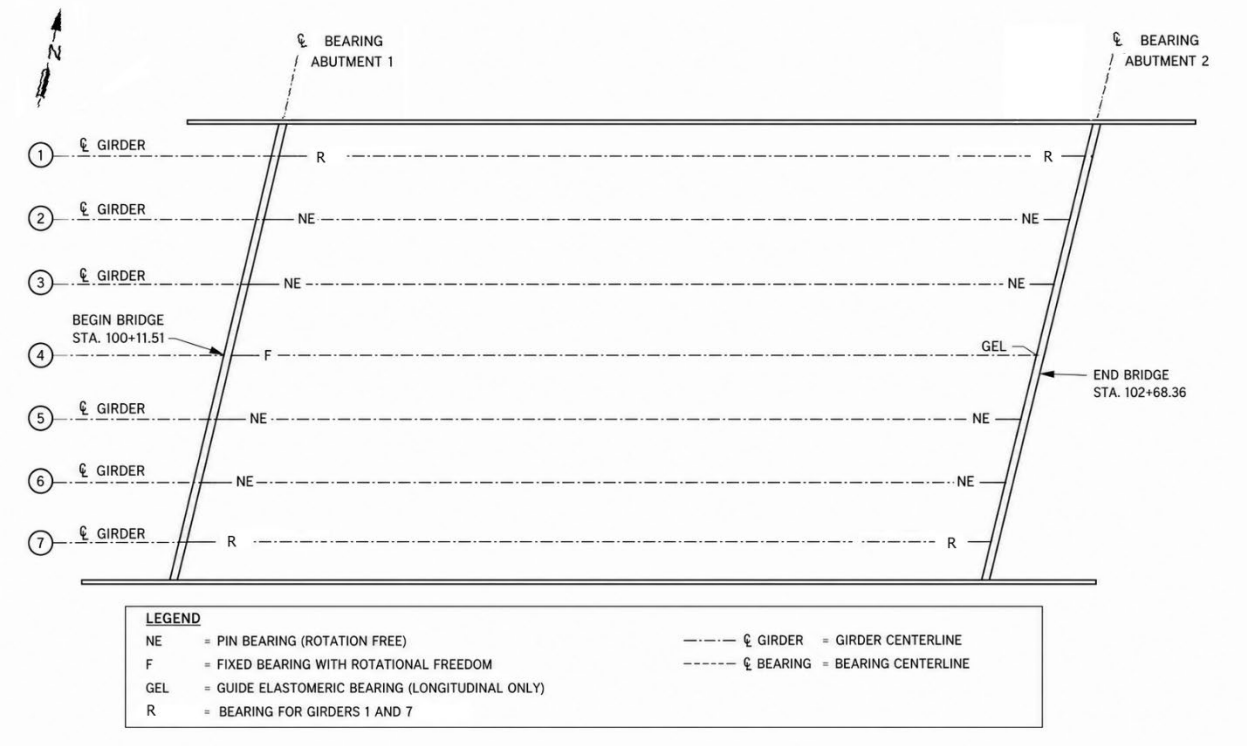

Figure 19. Bearing layout and support designations at girder ends.



(a) (b)

Figure 20. Bearing boundary conditions: (a) specialized roller support (R) for girders 1 and 7; (b) non-guided expansion (NE) bearing for girders 2, 3, 5, and 6.

In the finite element model, the global degrees of freedom consist of three translational components, U1, U2, and U3, corresponding to the longitudinal, vertical, and transverse directions, respectively, and three rotational components, UR1, UR2, and UR3, corresponding to rotations about the longitudinal (torsional), vertical, and transverse axes, respectively. Table 4 summarizes the translational (U) and rotational (UR) degrees of freedom restrained for each girder.

Table 4. Summary of finite element boundary condition constraints at girder supports.

Girder	Abutment 1	Abutment 2
1	U2, U3, UR1	U2, U3, UR1
2	U2	U2
3	U2	U2
4	U1, U2, U3	U2, U3
5	U2	U2
6	U2	U2
7	U2, U3, UR1	U2, U3, UR1

The R boundary condition consists of specialized roller bearings that restrain the transverse and vertical translations and torsional rotation while permitting longitudinal translation and rotational freedom. The finite element model approximates this boundary condition by restraining the vertical (U2) and transverse (U3) translations and torsional rotation (UR1) while permitting longitudinal translation (U1) and the remaining rotational degrees of freedom (UR2 and UR3), consistent with the behavior of the actual bearing. Girders 1 and 7 are supported by R bearings at both abutments.

The F boundary condition consists of a fixed bearing that restrains all translational degrees of freedom while permitting rotational freedom. This bearing provides the only restraint against longitudinal bridge movement and resists forces associated with braking, thermal effects, and other service loads. The finite element model approximates this boundary condition by restraining the longitudinal (U1), vertical (U2), and transverse (U3) translations while permitting all rotational degrees of freedom (UR1, UR2, and UR3), consistent with the behavior of the actual bearing. Girder 4 is supported by an F bearing at Abutment 1.

The GEL boundary condition consists of a longitudinally guided expansion bearing that permits longitudinal translation and rotational freedom while restraining the vertical and transverse translations. This bearing accommodates thermal expansion while maintaining the lateral stability of the bridge. The finite element model approximates this boundary condition by restraining the vertical (U2) and transverse (U3) translations while permitting longitudinal translation (U1) and all rotational degrees of freedom (UR1, UR2, and UR3), consistent with the behavior of the actual bearing. Girder 4 is supported by a GEL bearing at Abutment 2.

The NE boundary condition consists of a non-guided expansion bearing that permits longitudinal and transverse translations, as well as rotational freedom, while supporting the vertical load. This configuration accommodates thermal movements and other service-related deformations. In the finite element model, this boundary condition is approximated by restraining the vertical translation (U2) while permitting the longitudinal (U1) and transverse (U3) translations and all rotational degrees of freedom (UR1, UR2, and UR3), consistent with the behavior of the actual bearing. Girders 2, 3, 5, and 6 are supported by NE bearings at both abutments.

The ends of the arch ribs are anchored to the concrete thrust blocks through steel base plates and anchor rods secured with hex nuts, as shown in Figure 21. This anchorage system transfers the arch thrust to the supporting substructure while providing a high degree of restraint against both translational and rotational movements. Accordingly, the arch rib supports were idealized as fixed boundary conditions in the finite element model by restraining all translational (U1, U2, and U3) and rotational (UR1, UR2, and UR3) degrees of freedom.

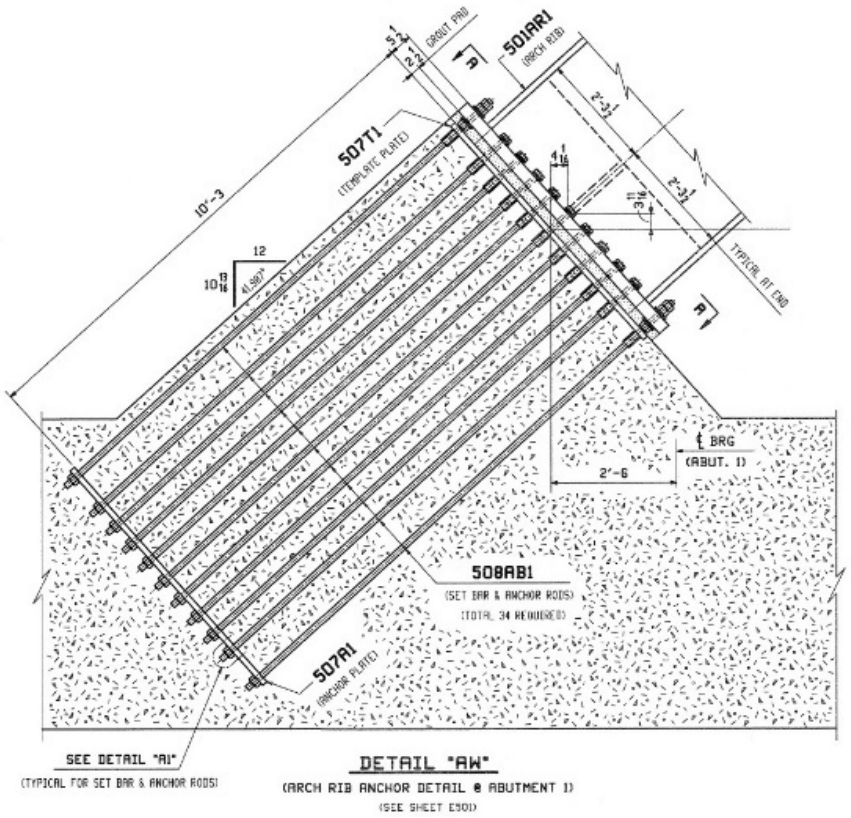

Figure 21. Arch rib anchorage details from the shop drawings, showing the base plate, anchor rods, and supporting system.

6.5 INTERACTIONS

Proper definition of interactions is essential for representing load-transfer mechanisms and connectivity among structural components in the finite element model. Two principal types of constraints available in Abaqus were employed in this model: tie constraints and pin-type multi-point constraints (MPCs). Built-up members, such as individual steel girders composed of multiple plates and stiffeners, were modeled as unified components. Consequently, internal interaction definitions were not required within these members, while continuity between their constituent parts was maintained.

All welded and bolted connections in the girders, floor beams, stiffeners, and connection plates were represented using tie constraints. This approach enforces displacement compatibility between adjoining surfaces and is commonly used to represent rigid structural connections. Individual bolts were not modeled to reduce model complexity and computational effort. The connections between the cable hangers and the supporting structural elements, including the arch ribs and floor beams, were represented using pin-type MPC constraints. This formulation permits rotational freedom while restraining translational degrees of freedom, thereby representing the behavior of pinned connections.

To simplify the model while preserving the intended structural behavior, the interaction between the concrete slab and the supporting steel structure was represented using tie constraints. Two slab-to-steel interaction assumptions were considered to investigate their influence on the dynamic characteristics of the bridge. In the first interaction type, Type 1, tie constraints were assigned to connect the edges of the floor beams and girders to the corresponding locations on the underside of the concrete slab. In the second interaction type, Type 2, tie constraints were assigned only at the floor beam locations, with no tie constraints assigned along the girders, resulting in less connectivity between the concrete deck and the steel structure than in Type 1. This approach assumes that composite action occurs primarily at the floor beam locations. The two interaction assumptions were subsequently evaluated as part of the finite element model updating procedure to assess their influence on the predicted modal properties of the bridge.

6.6 MESH

With the exception of the hanger cables, the entire bridge system was modeled using S4R shell elements in Abaqus. These four-node, reduced-integration shell elements with a finite membrane strain formulation provide an effective balance between accuracy and computational efficiency for large-scale structural analyses. Shell sections were defined with five integration points through the thickness to capture bending behavior and through-thickness stress variations in thin-walled components. Shell elements are capable of representing the axial, bending, and shear behavior of structural members.

To improve computational efficiency and simplify the model, the concrete slab was also represented using S4R shell elements. Because the reinforcing bars were not modeled, the slab was represented as a uniform concrete plate with a thickness of 9.5 in. This modeling approach captures the stiffness contribution and load distribution characteristics of the concrete deck. The mesh density was selected to maintain element aspect ratios close to one, thereby improving numerical stability and solution quality. The cable hangers were modeled using T3D2 truss elements, which carry axial forces only and do not resist bending moments or shear forces. The final finite element model consisted of 434,218 elements. Figure 22 illustrates the finite element mesh of the girders, floor beams, arch ribs, and concrete slab.

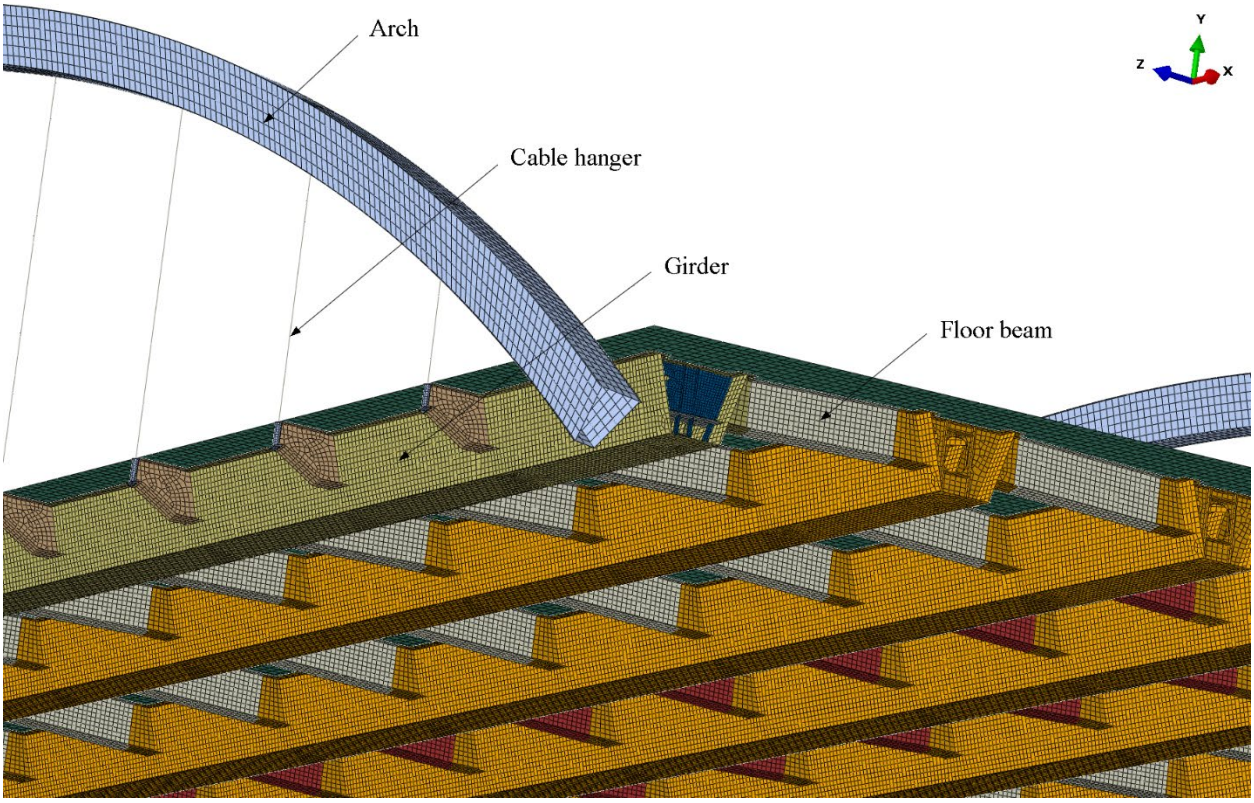

Figure 22. Perspective view of the finite element mesh for girders, floor beams, and arches.

6.7 LOCAL COORDINATE SYSTEMS

Rectangular local coordinate systems were assigned to the shell surfaces to facilitate the evaluation of stresses in the longitudinal and transverse directions of the structural components. Because the bridge consists of members with different orientations, the use of local coordinate systems ensures that the reported stress components are expressed relative to each structural element rather than the global coordinate system. This approach provides a consistent basis for evaluating stresses and comparing results among different bridge components.

For each shell surface from which stresses were extracted, the local coordinate system was oriented so that the 1-axis corresponded to the longitudinal direction of the member, the 2-axis corresponded to the transverse direction, and the n-axis was normal to the shell surface. Figure 23 illustrates examples of the rectangular local coordinate systems assigned to representative structural components. The corresponding global coordinate system is also shown for reference.

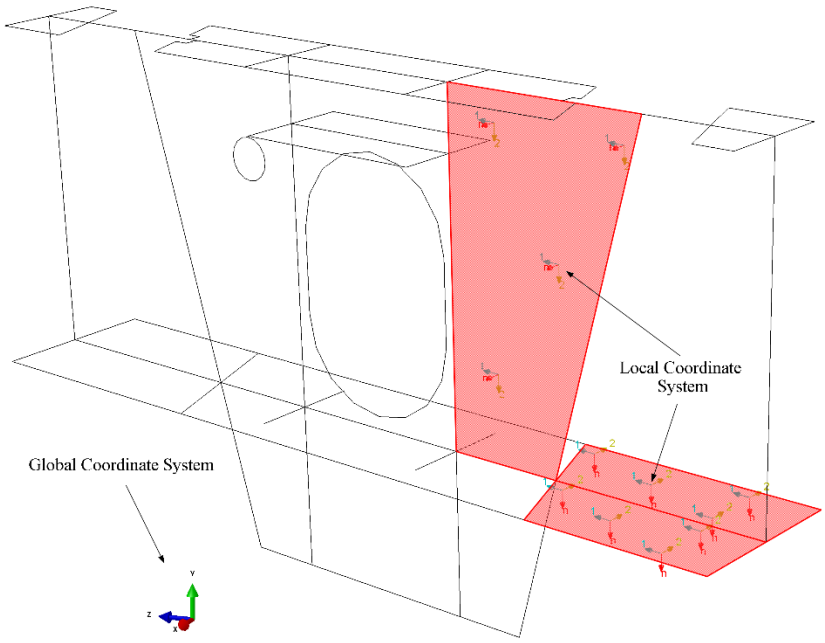

Figure 23. Representative local coordinate systems assigned to the shell surfaces for stress evaluation, along with the global coordinate system.

6.8 FINITE ELEMENT MODEL UPDATING

The finite element model was updated to improve the agreement between the initial numerical predictions and the measured dynamic response of the bridge. Although the initial model was developed based on the bridge geometry, material properties, and boundary conditions obtained from the design drawings, discrepancies may still exist between the numerical predictions and the experimentally identified modal properties. These discrepancies may arise from uncertainties in material properties, boundary conditions, connection behavior, composite action, and other modeling idealizations.

Frequency (eigenvalue) analysis was performed to determine the natural frequencies and corresponding mode shapes of the structure. Natural frequencies are the characteristic frequencies at which a structure vibrates after being disturbed from its equilibrium position, whereas mode shapes describe the corresponding deformation patterns. The eigenvalue problem determines these modal properties based solely on the structural mass and stiffness matrices. [19].

In Abaqus, frequency analysis is performed through eigenvalue extraction, in which the governing equations of motion are formulated as an eigenvalue problem using the structural mass and stiffness matrices. The subspace eigensolver with symmetric matrix storage was employed because of its suitability for large-scale finite element models and its computational

efficiency. The extracted eigenvectors were mass-normalized so that each mode had a unit generalized mass, thereby providing a consistent basis for modal analysis and comparison.

The results of a frequency analysis consist of eigenvalues, which correspond to the natural frequencies, and eigenvectors, which correspond to the mode shapes. Because the mode shapes are normalized, they do not represent actual displacement magnitudes but instead describe the relative deformation patterns of the structure. These modal properties were used to evaluate the dynamic characteristics of the bridge and to provide the numerical basis for comparison with the experimentally identified modal parameters.

6.8.1 Selection of modes for Comparison

The model updating procedure was performed using three experimentally identified vibration modes. Although additional modes were extracted from the finite element model, only those that could be reliably identified from the field measurements were considered. Modes dominated by arch-rib vibrations were excluded because of the limited quality of the measurements obtained from the sensors installed on the arch ribs. Furthermore, because the accelerometers recorded vibrations only in the vertical direction, only predominantly vertical vibration modes from the finite element model were selected for comparison. The selected experimental modes correspond to finite element Modes 3, 6, and 7.

6.8.2 Selection of Updating Parameters

Model updating involves adjusting parameters that significantly influence the predicted dynamic characteristics of the structure. For the I-20/59 McFarland Bridge, three updating parameters were selected based on their expected influence on the structural stiffness and modal properties. Two parameters corresponded to the elastic moduli of the structural materials, while the third parameter represented the interaction between the steel superstructure and the concrete deck, as described in Section 6.5.

Table 5 summarizes the 15 model updating cases investigated. The coefficient (k_s) represents the elastic modulus scaling factor applied to all steel components, while (k_c) represents the elastic modulus scaling factor applied to the concrete deck. fe_3, fe_6, and fe_7 denote the frequency errors for finite element Modes 3, 6, and 7, respectively, whereas MAC_3, MAC_6, and MAC_7 represent the corresponding MAC values.

Because the elastic modulus of steel (E_s) is well established and exhibits relatively little variability, its scaling factor was limited to a decrease of up to 2% from its nominal value. In contrast, the elastic modulus of concrete (E_c) may vary considerably because of aging, curing conditions, long-term material behavior, and cracking. Therefore, the elastic modulus of concrete was allowed to decrease by up to 50% from its nominal value.

6.8.3 Model Updating Criteria

The experimentally identified modal properties, including the natural frequencies and mode shapes obtained from field vibration measurements, were used as the reference data for the model updating procedure. The relative frequency error was used to quantify the difference between the experimental and numerical frequencies, whereas the MAC was used to quantify the similarity between the experimental and numerical mode shapes. A MAC value close to 1.0 indicates strong agreement between the measured and predicted mode shapes, whereas a value close to 0 indicates poor correlation. The MAC was calculated using Equation (4).

$$(4)\ MAC_i(\alpha) = \frac{\left((\psi_i^{EXP})^T \psi_i(\alpha)\right)^2}{\|\psi_i^{EXP}\|_2^2 \|\psi_i\|_2^2},\ i = 1 \dots n_{Modes}$$

Where:

ψ_i^{EXP} is the experimental mode shape vector

$\psi_i(\alpha)$ is the corresponding numerical mode shape vector

To quantify the agreement between the numerical and experimental modal properties, an objective function based on both the natural frequency error and the mode shape correlation was defined. The objective function is expressed as

$$(5)\ J = \frac{1}{N_m} \sum_{i=1}^{N_m} \left[\frac{|f_i^{FE} - f_i^{EXP}|}{f_i^{EXP}} + (1 - MAC_i) \right]$$

Where:

J is the objective function value

N_m is the number of modes considered

f_i^{FE} and f_i^{EXP} are the numerical and experimental natural frequencies of mode *i*, respectively

MAC_i is the MAC associated with mode *i*

The first term in Equation (5) quantifies the relative frequency error, whereas the second term quantifies the discrepancy between the numerical and experimental mode shapes. Consequently, smaller objective function values indicate better agreement between the numerical and experimental modal properties. However, the objective function alone is not sufficient for selecting the best updated model. Therefore, the frequency errors, MAC values, and physical plausibility of the updated material properties were also considered during the model selection process.

6.8.4 Selection of the Updated Model

The updated model was selected by considering several criteria, including frequency errors below 5%, MAC values greater than 0.9, a low objective function value, and material property modifications that remained as close as possible to their nominal values. A summary of all cases considered, and their frequency error (*fe*), MAC values, and objective function values is included in Table 5.

Table 5. Summary of finite element model updating results.

No.	Interaction Type	k_s	k_c	fe_3 (%)	fe_6 (%)	fe_7 (%)	MAC_3	MAC_6	MAC_7	Objective Function Value
1	Type 1	1	1	9.00	1.88	1.62	0.9915	0.9694	0.9297	0.0781
2	Type 1	1	0.9	7.95	0.73	2.31	0.9910	0.9687	0.9298	0.0735
3	Type 1	1	0.8	6.73	0.56	3.09	0.9903	0.9679	0.9299	0.0719
4	Type 1	1	0.7	5.31	2.04	3.96	0.9894	0.9666	0.9300	0.0757
5	Type 1	1	0.6	3.59	3.75	4.95	0.9882	0.9648	0.9300	0.0800
6	Type 1	1	0.5	1.46	5.76	6.10	0.9867	0.9622	0.9299	0.0848
7	Type 1	0.99	0.7	4.89	2.42	4.38	0.9894	0.9667	0.9300	0.0769
8	Type 1	0.99	0.6	3.18	4.12	5.36	0.9883	0.9650	0.9300	0.0811
9	Type 1	0.99	0.5	1.07	6.13	6.51	0.9868	0.9624	0.9299	0.0860
10	Type 1	0.98	0.7	4.46	2.80	4.79	0.9895	0.9668	0.9300	0.0781
11	Type 1	0.98	0.6	2.77	4.50	5.78	0.9884	0.9651	0.9300	0.0823
12	Type 1	0.98	0.5	0.68	6.49	6.92	0.9869	0.9625	0.9299	0.0872
13	Type 2	0.98	0.7	5.10	3.51	5.94	0.9897	0.9642	0.9270	0.0882
14	Type 2	0.98	0.6	3.40	5.11	6.85	0.9885	0.9621	0.9259	0.0924
15	Type 2	0.98	0.5	1.30	6.99	7.92	0.9869	0.9592	0.9235	0.0975

As shown in Table 5, Cases 4, 7, and 10 differ only in the elastic modulus of steel. As the steel elastic modulus was reduced from its nominal value (k_s = 1.0) to 0.99 and 0.98, the frequency error for Mode 3 decreased from 5.31% to 4.89% and 4.46%, respectively. However, the frequency errors for Modes 6 and 7 increased from 2.04% and 3.96% to 2.42% and 4.38%, and then to 2.80% and 4.79%, respectively. Consequently, the objective function increased slightly from 0.0757 to 0.0769 and 0.0781. These results indicate that reducing the elastic modulus of steel improves the correlation for Mode 3 but degrades the agreement for Modes 6 and 7, resulting in a less favorable overall agreement with the experimental modal properties.

Cases 13, 14, and 15 have the same material-property assumptions as cases 10, 11, and 12, respectively, but different slab-to-steel interaction models. The frequency errors and objective function values for these cases increased. These results indicate that the reduced slab-to-steel connectivity assumed in the Type 2 interaction does not improve the agreement between the numerical and experimental modal properties and may not adequately represent the actual

composite behavior of the bridge. Therefore, the Type 1 interaction assumption provided the most realistic representation of the composite behavior between the steel superstructure and the concrete deck of the two connectivity types considered.

Cases 5, 7, and 10 were identified as the most suitable candidates for the final updated model because they satisfied the frequency error criterion of less than 5% for all three selected modes while maintaining MAC values greater than 0.9. Case 5 was selected as the final updated model for all subsequent analyses because it achieved satisfactory agreement with the experimentally identified modal properties while requiring a smaller reduction in the concrete elastic modulus and maintaining the steel elastic modulus at its nominal value. For case 5, the elastic modulus scaling factors were $k_s = 1.0$ and $k_c = 0.6$, corresponding to no reduction in the steel elastic modulus and a 40% reduction in the concrete elastic modulus. The resulting frequency errors for finite element Modes 3, 6, and 7 were 3.59%, 3.75%, and 4.95%, respectively, while the corresponding MAC values were 0.9882, 0.9648, and 0.9300. The corresponding objective function value was 0.0800.

6.8.5 Natural Frequencies and Mode Shapes

The modal properties of the final updated finite element model, including the natural frequencies and corresponding periods, are presented in Table 6 for the first nine vibration modes. The first two modes exhibit nearly identical natural frequencies of 0.7701 Hz, forming a closely spaced modal pair. Despite their similar frequencies, their mode shapes are distinct, indicating different vibration characteristics.

Table 6. Modal properties of the final updated finite element model.

Mode	Frequency (Hz)	Period (s)	Description
1	0.7701	1.2985	Asymmetric lateral arch sway
2	0.7701	1.2985	Symmetric lateral arch sway
3	1.5012	0.6661	Global deck bending
4	2.2042	0.4537	First higher-order arch deformation mode
5	2.2042	0.4537	Second higher-order arch deformation mode
6	2.4563	0.4071	Coupled arch–deck bending
7	2.9080	0.3439	Coupled deck torsion and arch deformation
8	3.1585	0.3166	Complex coupled arch–deck deformation
9	3.5068	0.2852	Coupled deck bending and torsion

Figure 24 illustrates the first nine vibration mode shapes. As shown, the first two modes are dominated by lateral vibrations of the arch ribs, with each exhibiting a distinct deformation pattern that is likely associated with symmetric and antisymmetric behavior.

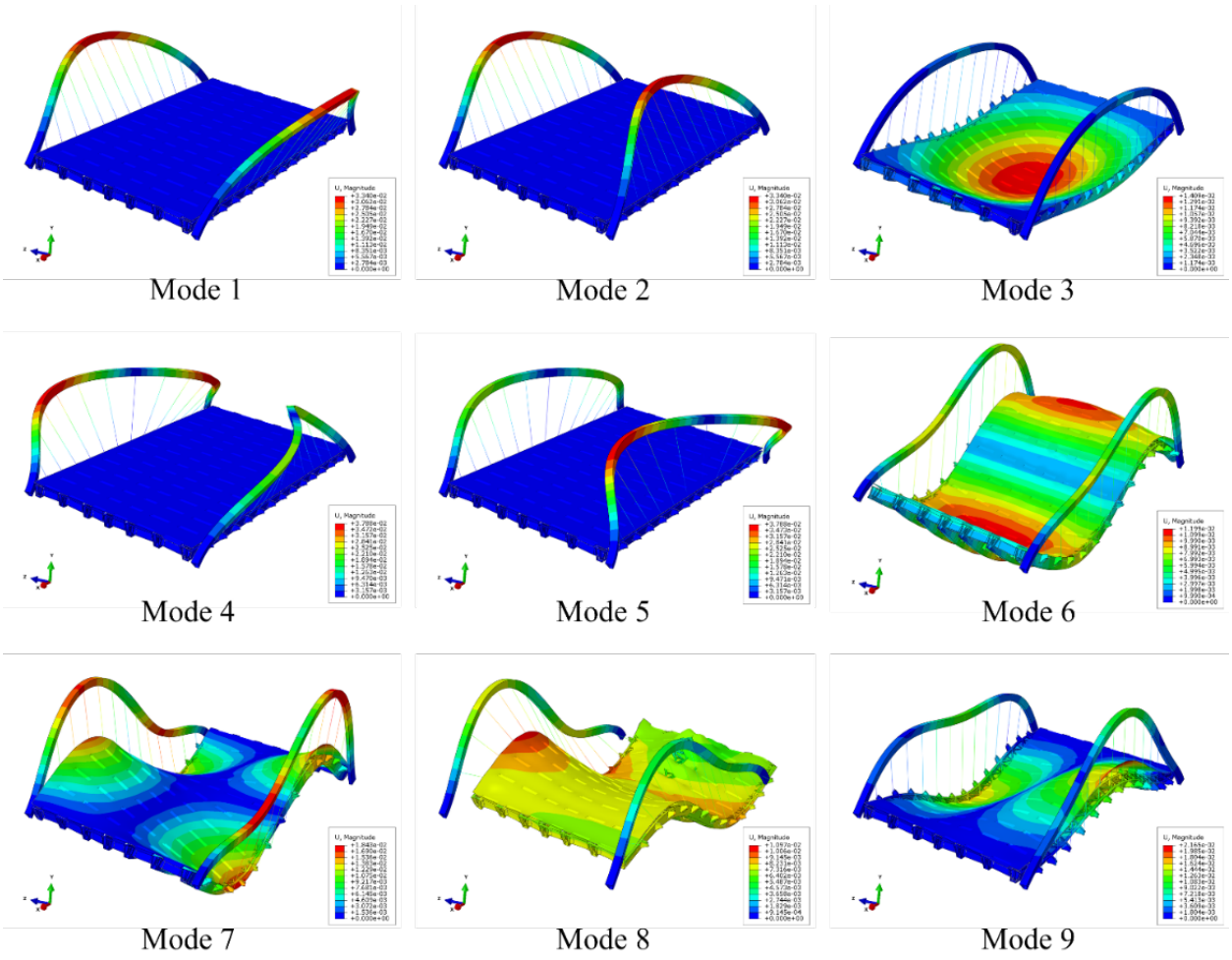

Figure 24. First nine vibration mode shapes obtained from the Abaqus eigenvalue analysis.

Mode 3, with a natural frequency of 1.5012 Hz, is predominantly characterized by deformation of the bridge deck and longitudinal girders. The mode exhibits a global bending response with maximum deflection occurring near midspan, while the arch ribs contribute less to the overall deformation than in the first two modes. This mode marks the transition from arch-dominated vibration to global deformation involving greater participation of the bridge deck.

Modes 4 and 5 also form a closely spaced modal pair and are primarily associated with deformation of the arch ribs. In contrast, Modes 6 through 9 exhibit coupled deformation of the arch ribs and the bridge deck, reflecting increased interaction between the primary structural components at higher vibration modes.

CHAPTER 7 - FATIGUE LIFE ESTIMATION

7.1 FATIGUE LOADING

For fatigue analysis, the bridge was subjected to the AASHTO LRFD fatigue live load specified in Article 3.6.1.4.1 [6]. For non-orthotropic bridge decks like that present in the I-20/59 McFarland bridge, fatigue loading consists of one AASHTO design truck as defined in Article 3.6.1.2.2. The characteristics of the fatigue design truck are described in Section 3.2.

To account for the movement of traffic loads, each axle load was multiplied by the dynamic load allowance factor, *IM*, of 1.15 as specified in the AASHTO *LRFD BDS*. The resulting axle loads are summarized in Table 7. The lane factor, *p*, specified in Article 3.6.1.4.2 was not applied to the fatigue truck loading because it is used to estimate the single-lane average daily truck traffic ($ADTT_{SL}$) for fatigue life calculations rather than to modify the magnitude of the fatigue design truck. Accordingly, the fatigue design truck was applied using the axle loads specified in Article 3.6.1.4.1, while the lane factor was considered separately in the fatigue life calculations.

Table 7. Fatigue design truck wheel loads and applied contact pressures.

Axle	Axle Load (kip)	Tire Force (kip)	Contact Area (in²)	Pressure (psi)
Rear (32 kip)	36.8	18.4	200	92 psi
Front (8 kip)	9.2	4.6	100	46 psi

The wheel loads were applied to the bridge deck through six rigid plates representing the tire contact areas. Based on the AASHTO fatigue truck footprint, a contact area of 200 in^2 was assigned to each the four rear tires and 100 in^2 contact area was assigned to each of the two front tires. Consequently, uniform pressures of 92 psi and 46 psi were applied to the rear and front rigid plates, respectively. Each rigid plate was connected to the bridge deck using a tie constraint, ensuring full transfer of the wheel loads to the deck.

To facilitate moving the truck to different longitudinal positions without redefining individual wheel locations, all six rigid plates were connected to a single reference point (RP) located at the center of gravity (CG) of the loading system. Based on the axle configuration of the fatigue design truck, the CG is located 25.78 ft behind the centerline of the front axle (or equivalently 18.22 ft ahead of the rear axle group), as illustrated in Figure 25. By translating this RP, the entire loading system could be repositioned efficiently while maintaining the correct relative spacing between the wheel loads.

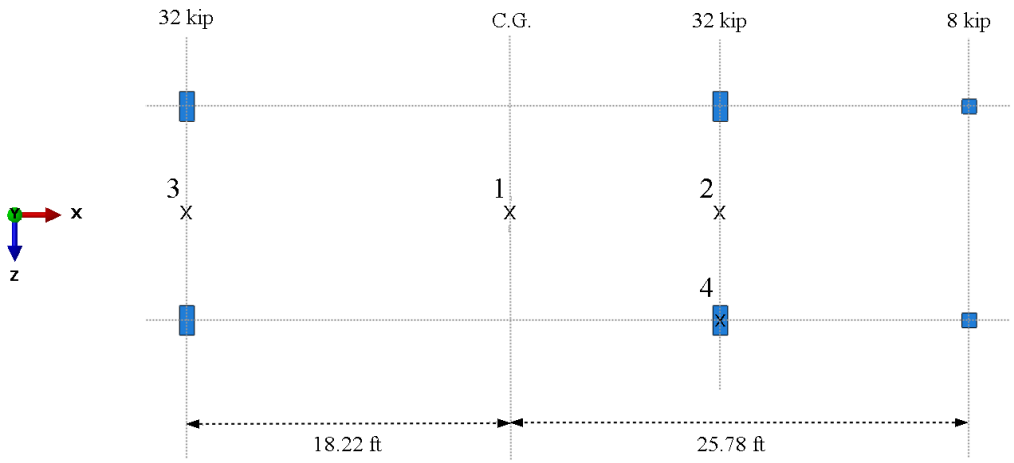

Figure 25. Fatigue loading scenarios adopted to maximize the stress response at different stress measurement points.

Since the fatigue details investigated in this project are located at different positions on the bridge, a single truck location does not necessarily produce the maximum stress range at every detail. Therefore, four different loading scenarios were considered for each fatigue detail to obtain the maximum possible stress response as required by the AASHTO LRFD BDS. The loading scenarios are illustrated in Figure 25. In loading scenario 1, the truck was positioned by placing the center of gravity (CG) of the loading system at the selected load location. In loading scenarios 2, 3, and 4, the truck was positioned such that Points 2, 3, and 4, respectively, were placed at the selected global load positions (A, B, C, or D, as described following). This approach allowed the stress to be evaluated for each detail of interest with the fatigue truck positioned at four representative longitudinal positions while maintaining the prescribed axle spacing and wheel configuration.

Most of the fatigue-sensitive details were located near the diaphragms, the connections between the floor beams and the main girders, and the splice locations. Therefore, four load positions were selected, as shown in Figure 26. Load position A is at midspan of floor beam 8 between main girders 4 and 5. Load position B is directly above the splice at the midspan of main girder 4 between floor beams 6 and 7. Similarly, load position C is at the midpoint of the diaphragm at the intersection of main girder 4 and floor beam 8. Load position D is at the midspan of the main girder 4 between floor beams 8 and 9.

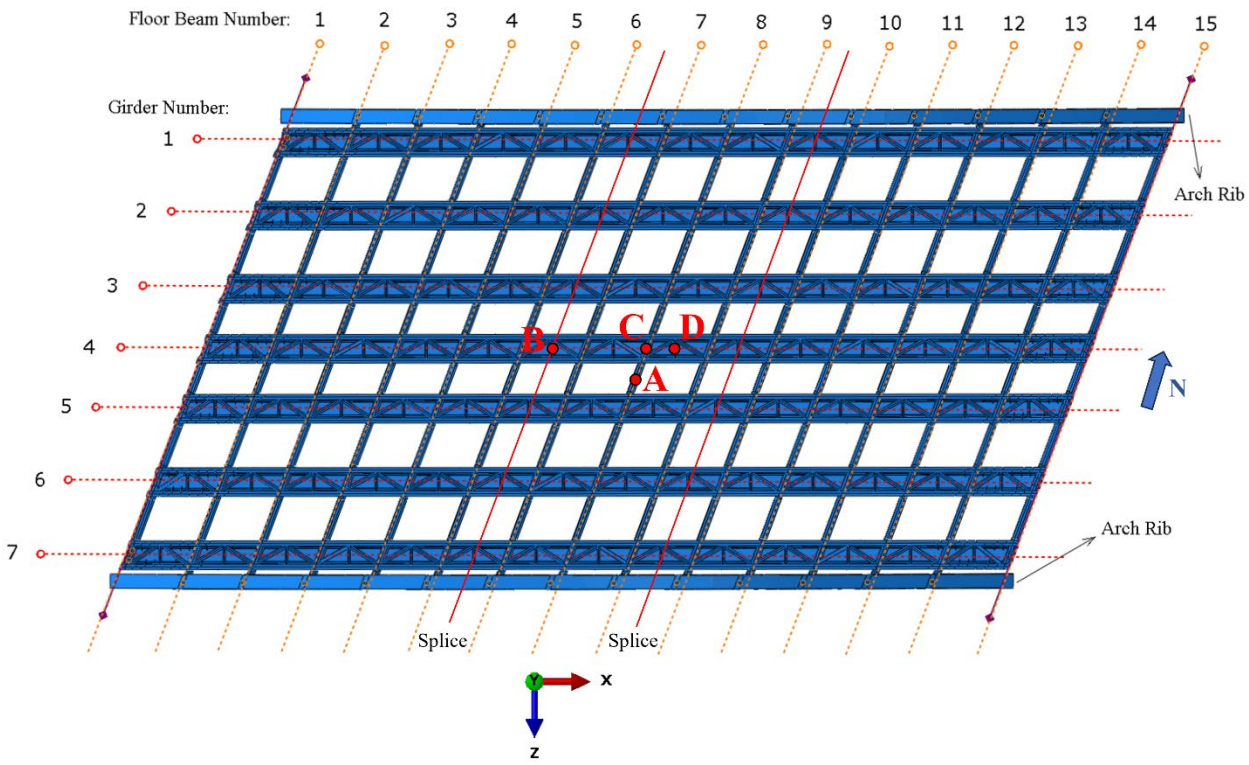

Figure 26. Global load positions on main girder 4.

The fatigue truck load was also applied to the corresponding stress points on the edge girder (main girder 7) to evaluate if the stresses at the fatigue sensitive details discussed in Section 7.3 following may be higher under a torsional load. For main girder 7, load position A is at midspan of floor beam 8 between main girders 6 and 7. Load position B is directly above the splice at the midspan of main girder 7 between floor beams 6 and 7. Similarly, load position C is at the midpoint of the diaphragm at the intersection of main girder 7 and floor beam 8. Load position D is at the midspan of the main girder 7 between floor beams 8 and 9.

7.2 FATIGUE SENSITIVE DETAILS

The fatigue sensitive details present in the I-20/59 McFarland bridge were identified based on Table 6.6.1.2.3-1 of AASHTO *LRFD BDS*. All details present on the bridge were compared with the details listed in Table 6.6.1.2.3-1 to identify their corresponding fatigue detail categories. Once the fatigue detail category was established, the respective fatigue growth constant, m, constant amplitude fatigue threshold, and detail constant, A, could be obtained to predict the fatigue life. A total of 13 points of interest were identified for fatigue life estimation as shown in Table 8. The stress points shown in Table 8 and described following are centered around main girder 4, but the corresponding points were also assessed for main girder 7. Because accelerometer data from the arches was not reliable and was not used to update the model, fatigue sensitive details present in the arches were not considered for remaining fatigue life calculations.

Table 8. Identified fatigue sensitive details.

Stress Point	Detail Category	Section of Table 6.6.1.2.3-1	Load Location
1	B	3.1	A
2	B	2.1	A
3	B	2.1	B
4	B	2.1	B
5	B	3.1	B
6	B	2.1	C
7	D	1.5	C
8	C	5.4	C
9	C	5.4	C
10	C	5.4	C
11	B	2.1	C
12	B	3.1	C
13	A	1.1	D

From load location A as shown in Figure 27, the stress in the bottom flange of the floor beam was obtained which corresponds to section 3.1 of Table 6.6.1.2.3-1 in the AASHTO LRFD BDS and falls into detail category B. The same load location was also used to determine stress near the bolted connections between the main girders and floor beams, which corresponds to table section 2.1 and falls into detail category B. The locations of these stress points are shown in Figure 28.

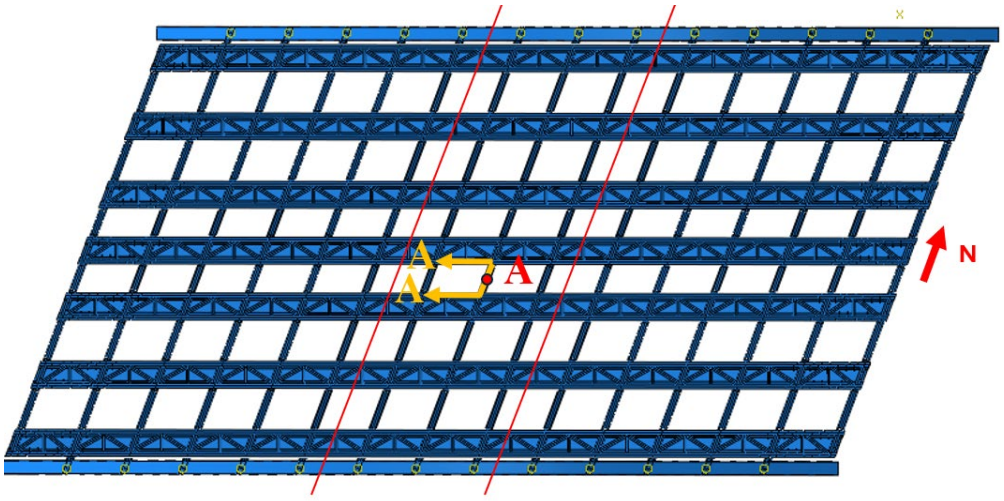

Figure 27. Load location A.

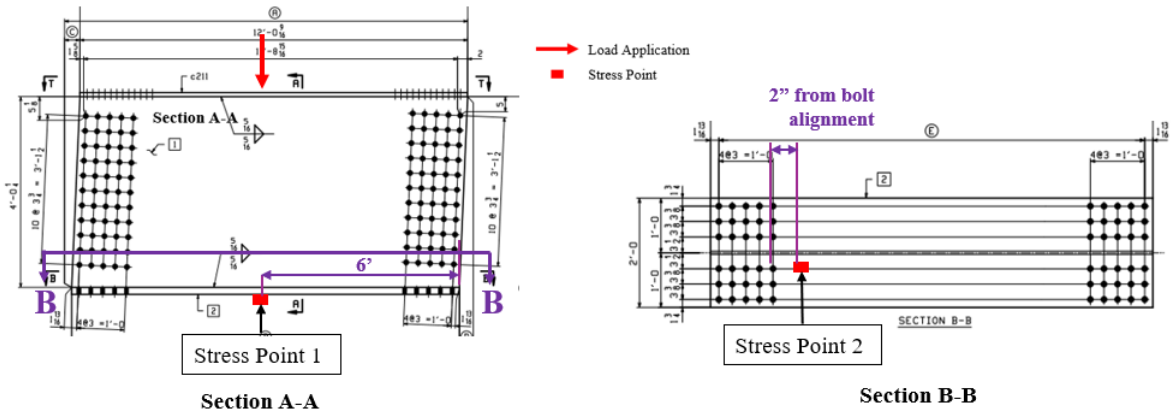

Figure 28. Details of stress points from load location A.

From load location B as shown in Figure 29, the stress near the bolted splice connection of the main girder and the bolted connection between top flange of main girder and the lateral braces was determined. These details correspond to table section 2.1 and fall into detail category B. Stress near the longitudinal welded joint between bottom flange and web of the main girder was determined from the same load location, which corresponds to table section 3.1 and falls into detail category B. The locations of these stress points are shown in Figure 30.

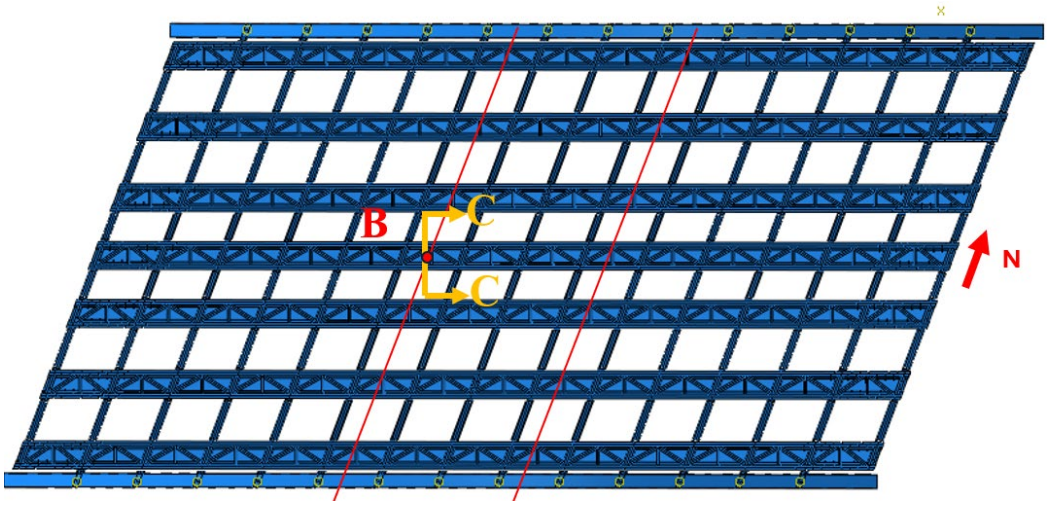

Figure 29. Load location B.

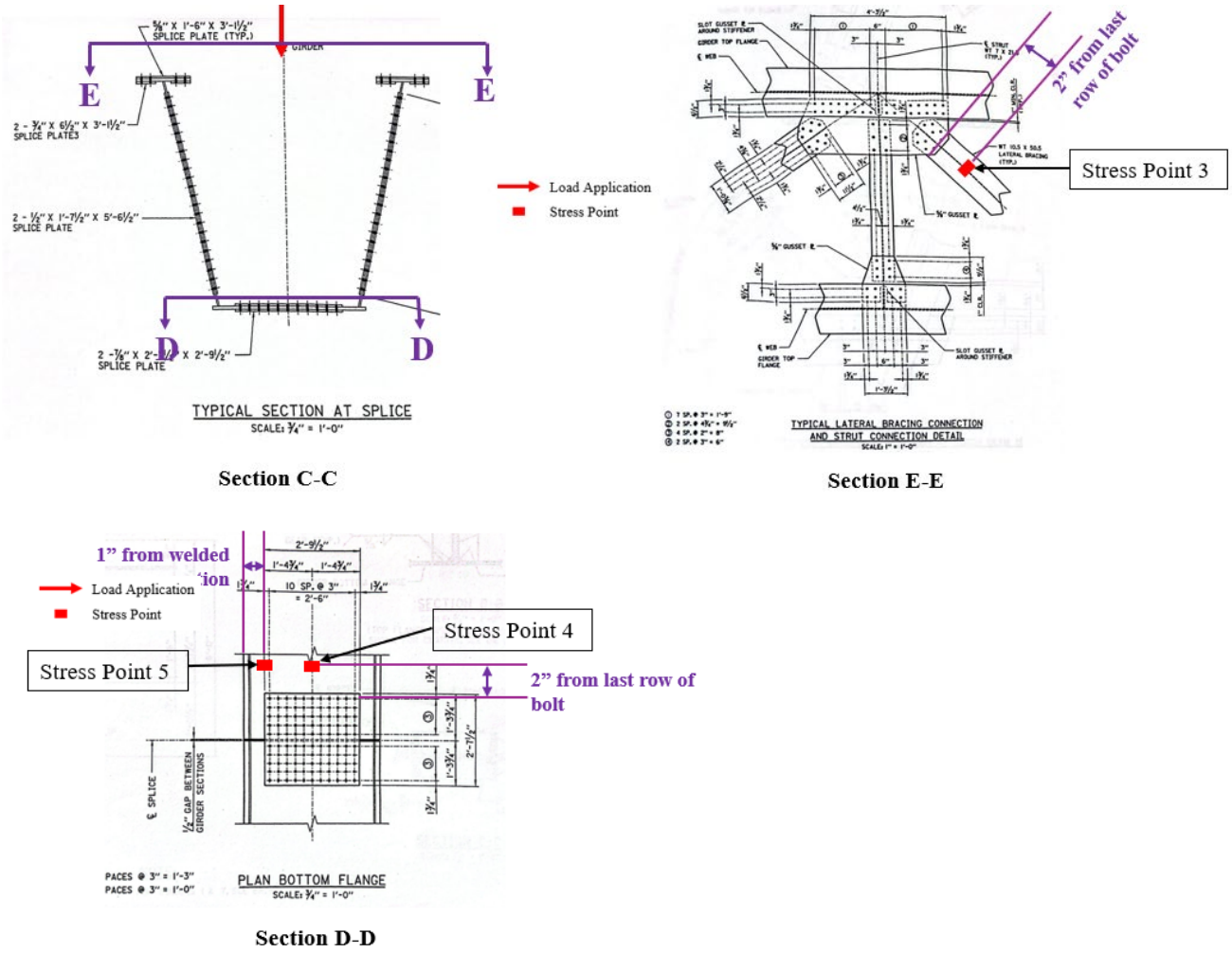

Figure 30. Details of stress points from load location B.

From load location C as shown in Figure 31, the stresses at the various locations on the diaphragm corresponding to table section 5.4 and fatigue category C were obtained. The stress near the conduit opening in the diaphragm, which corresponds to table section 1.5 and fatigue category D, was also obtained from this loading case. In addition, the stresses in the connection regions between the main girders and floor beams were determined. Since both bolted and welded connections are present in this region, they correspond to table section 2.1 and 5.4 and fatigue category B and C, respectively. This location was also suitable for obtaining stress in the bottom flange of the main girder near the welded connection between the web and bottom flange. The locations of these stress points are shown in Figure 32.

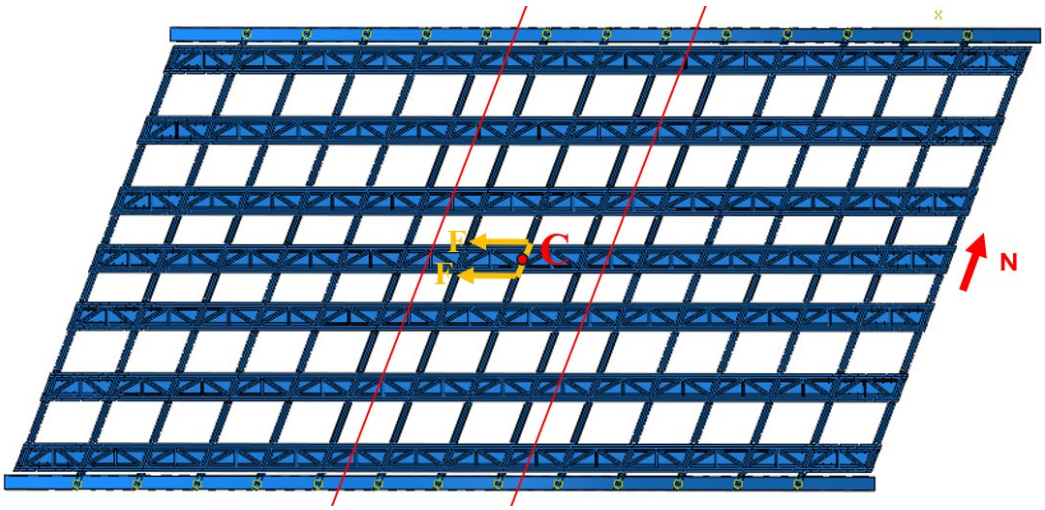

Figure 31. Load location C.

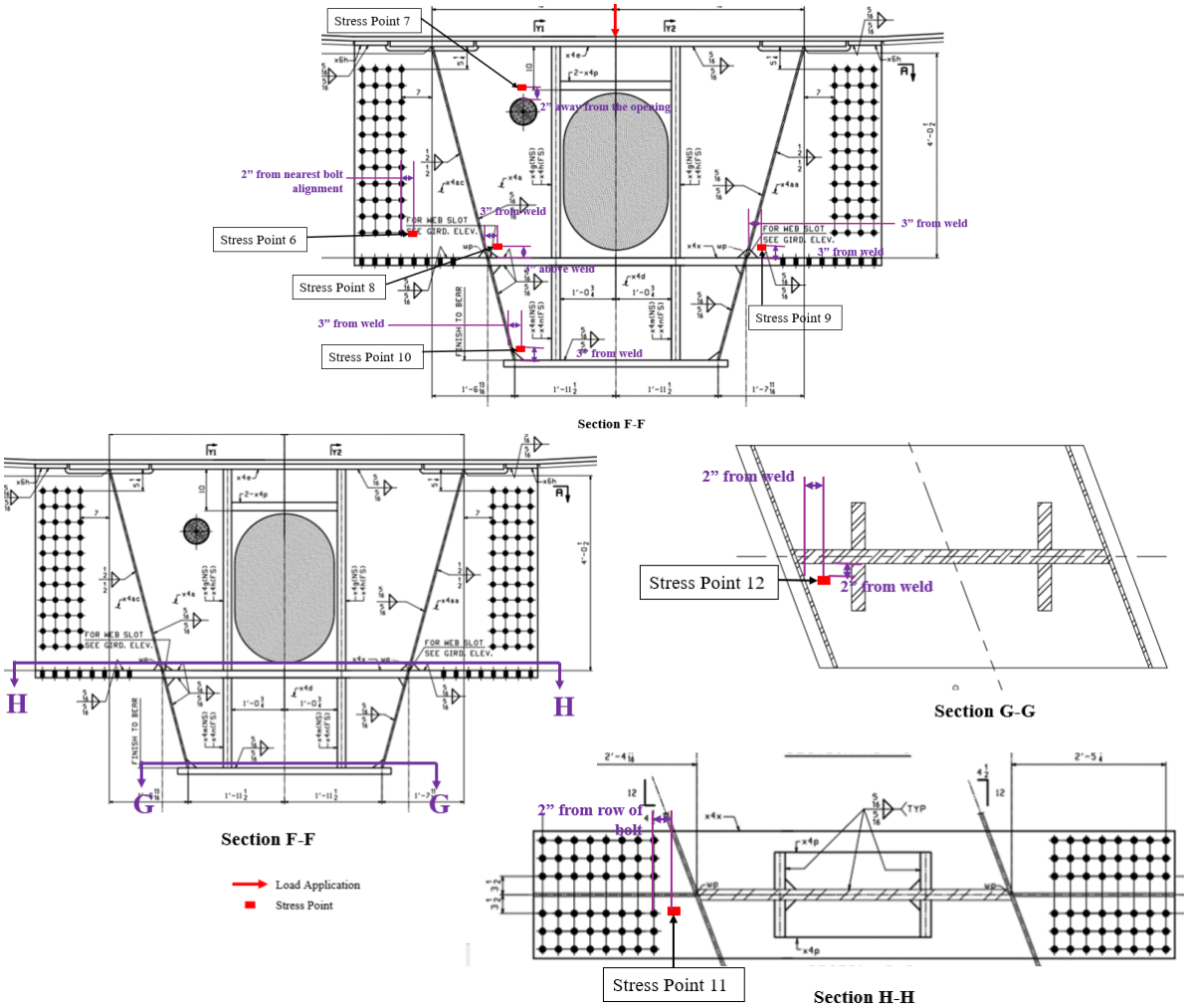

Figure 32. Details of stress points from load location C.

From load location D as shown in Figure 33, the stress at the midspan of bottom flange of main girder, away from any welded joints, was obtained. This detail corresponds to table section 1.1 and falls into detail category A. The location of this stress point is shown in Figure 34.

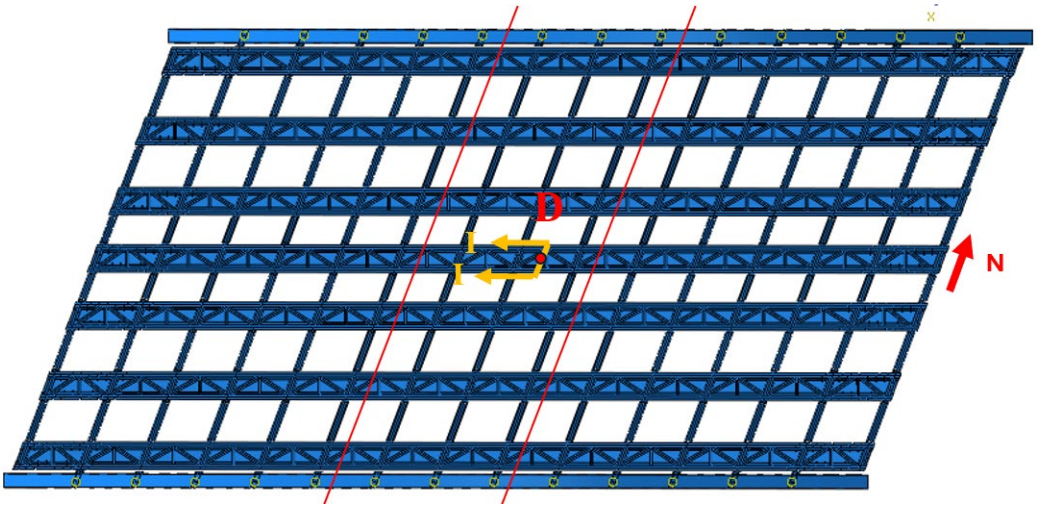

Figure 33. Load location D.

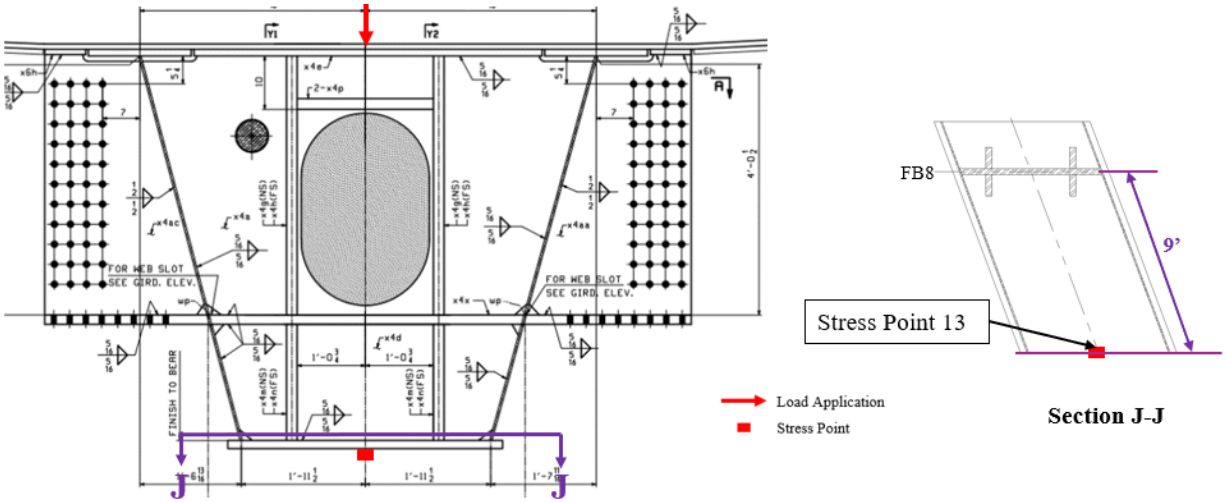

Figure 34. Details of stress points from load location D.

7.3 FATIGUE LIFE ESTIMATION

The fatigue load, according to AASHTO LRFD BDS, was applied to the finite element model at the load positions discussed in Sections 7.1 and the maximum stress at the points of interest was extracted. The points of interest, their corresponding detail category and CAFT, and the

maximum stress values from loading centered around main girders 4 and 7 are presented in Table 9.

Table 9. Summary of maximum stress values.

Stress Point	Detail Category	CAFT (ksi)	Maximum stress from model (ksi)	
			Main Girder 4	Main Girder 7
1	B	16	1.36	0.92
2	B	16	1.28	1.01
3	B	16	0.3	0.07
4	B	16	0.55	0.36
5	B	16	0.55	0.36
6	B	16	0.96	0.41
7	D	7	0.33	0.51
8	C	10	0.5	0.24
9	C	10	1.34	0.82
10	C	10	0.02	0.03
11	B	16	1.24	0.58
12	B	16	0.79	0.23
13	A	24	0.55	0.42

For all the details, the maximum stress is less than the CAFT. This indicates that all details investigated have an infinite fatigue life.

Additionally, the location and magnitude of the maximum stress in the overall bridge model were also checked for each loading case to identify any missing fatigue-critical details in the bridge. From these checks, the maximum stress, with a value of 11.67 ksi, was found to be located near the bolted connection between the upper flange of floor beam 5 and main girder 7, as denoted by maximum stress point 14 in Figure 35 and Figure 36, when the truck load location was B and loading scenario 4 for main girder 7. This bolted connection corresponds to table section 2.1 in Table 6.6.1.2.3-1 of AASHTO LRFD BDS 10th edition which has a category B and fatigue threshold value of 16 ksi. This suggests that the fatigue detail experiencing the maximum stress range also has an infinite fatigue life.

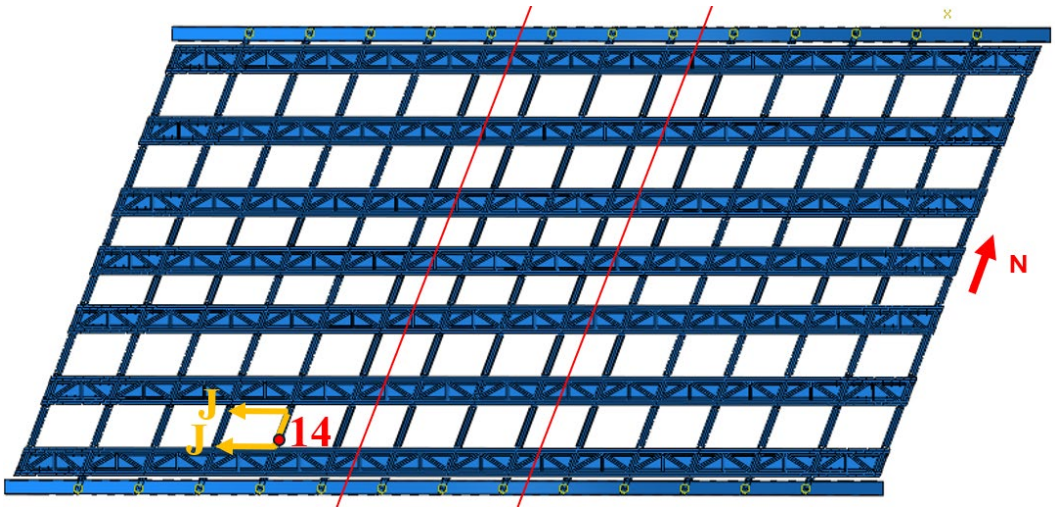

Figure 35. Location of maximum stress point.

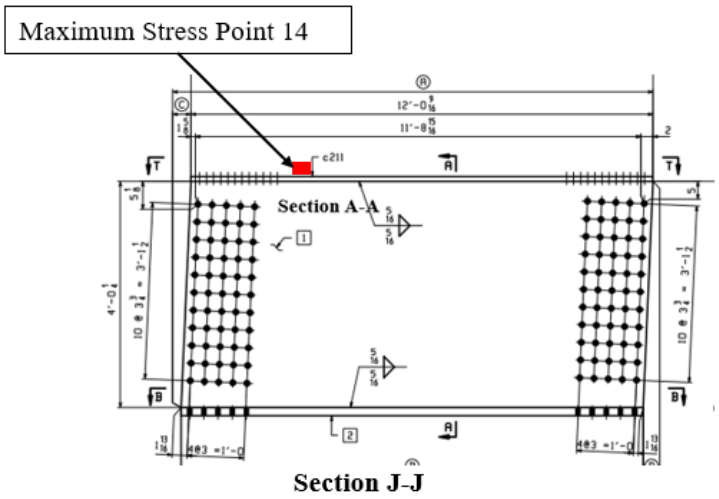

Figure 36. Detail of maximum stress point at the connection of floor beam 5 and main girder 7.

CHAPTER 8 - CONCLUSIONS AND RECOMMENDATIONS

8.1 CONCLUSIONS

In support of the project objectives to (1) conduct long-term monitoring, (2) develop and update a finite element model of the bridge using field measurements, and (3) evaluate the life of fatigue-sensitive details, long-term monitoring of the acceleration of the bridge deck was successfully completed from October 2025 through February 2026. More than 2,000 acceleration records were collected through an automated monitoring system. Modal analysis successfully identified the bridge's natural frequency and key modal characteristics from the bridge deck accelerometer data.

A detailed three-dimensional finite element model of the I-20/59 McFarland Bridge was developed based on the bridge design and shop drawings. The model was successfully calibrated against the experimentally identified modal properties by maintaining the structural steel elastic modulus at 100% of its nominal value, reducing the concrete deck elastic modulus to 60% of its nominal value, and assuming fully composite interaction between the steel superstructure and the concrete deck. The selected updated model achieved frequency errors of 3.59%, 3.75%, and 4.95% for the three selected vibration modes, with corresponding MAC values of 0.9882, 0.9648, and 0.9300, resulting in an objective function value of 0.0800. The updated model demonstrated good agreement with the experimentally identified modal properties and was subsequently adopted for fatigue life predictions.

Thirteen fatigue-sensitive details were identified and assessed around main girders 4 and 7. The maximum stress ranges of these details were evaluated using the fatigue truck loading from the AASHTO LRFD BDS and the updated finite element model. The maximum stress ranges for all details identified, including the maximum stress location, were below the CAFT for the corresponding detail category, indicating that all details on the bridge have an infinite fatigue life. Based on the fatigue life predictions from the updated finite element model, the I-20/59 McFarland Bridge is not predicted to be susceptible to load-induced fatigue damage.

8.2 IMPLEMENTATION FOR ALDOT

- Re-instrument the bridge arches with accelerometers to capture the global acceleration behavior of the bridge.

- During routine bridge inspections, prioritize visual inspection of the fatigue-sensitive details identified in Section 7.2.

- Repeat the fatigue assessment if future traffic volumes or operating conditions differ significantly from the assumptions used in this study.

- Apply the monitoring and model-updating framework developed in this project to other bridges in Alabama to support statewide bridge asset management efforts.

8.3 FUTURE RESEARCH

- Instrument the bridge with strain gages at the selected fatigue sensitive details to directly measure the stress ranges under actual traffic loading to further validate the fatigue assessment.

- Extend the monitoring period to evaluate the long-term stability of the bridge's dynamic characteristics under varying environmental and operational conditions.

- Investigate the effect of seasonal traffic variations, including University of Alabama football game traffic, on truck traffic volumes.

ACKNOWLEDGEMENTS

The material in this report was obtained in connection with the research project, "Condition Assessment of Steel Box Girder Bridge Using Long-Term Field Measurements," Alabama Department of Transportation (ALDOT) Project 930-972, conducted by the University of Alabama. Funding for the project was provided by ALDOT. The funding, cooperation, and assistance of many individuals from each of these organizations are gratefully acknowledged. The authors particularly acknowledge the contributions of the following individuals for serving on the research advisory committee and assisting with sensor installation and maintenance:

Kidada Dixon	ALDOT, RAC Chair
Clay McBrien	ALDOT, RAC Vice-Chair
Edward Austin	ALDOT, RAC Member
Stan Biddick	ALDOT, RAC Member
Scott George	ALDOT, RAC Member
Eric Christie	ALDOT, RAC Member
DeJarvis Leonard	ALDOT, RAC Member
Stacey Glass	ALDOT, RAC Member
Brad Lindsey	ALDOT, RAC Member
Brad Williams	ALDOT, RAC Member
Eric Christie	ALDOT, RAC Member
Ramy Abdalla	ALDOT, Engineer
Berhanu Woldemichael	ALDOT, Engineer
Robert Maxwell	ALDOT, ITS Manager
Evan Clark	Bridge Diagnostics, Inc., Project Manager
Jesse Sipple	Bridge Diagnostics, Inc., VP
Lincoln Smith	Bridge Diagnostics, Inc., Application Support Technician

REFERENCES

[1] T. Helwig, J. Yura, R. Herman, E. Williamson, and D. Li, "Design Guidelines for Steel Trapezoidal Box Girder Systems," Center for Transportation Research, Austin, TX, FHWA/TX-07/0-4307-1, Apr. 2007.

[2] D. H. Hall, "Why Steel Box Girders?," National Steel Bridge Alliance, 6, Apr. 1997.

[3] J. W. Fisher, *Fatigue and Fracture in Steel Bridges*. Wiley, 1984.

[4] X. W. Ye, Y. H. Su, and J. P. Han, "A State-of-the-Art Review on Fatigue Life Assessment of Steel Bridges," *Mathematical Problems in Engineering*, vol. 2014, no. 1, p. 956473, Jan. 2014, doi: 10.1155/2014/956473.

[5] S.-B. Lee, "Fatigue Failure of Welded Vertical Members of a Steel Truss Bridge," *Engineering Failure Analysis*, vol. 3, no. 2, pp. 103–108, Jun. 1996, doi: 10.1016/1350-6307(96)00003-9.

[6] AASHTO, *LRFD Bridge Design Specifications*, Washington, DC 20004., 2024.

[7] Y. Wang, R. J. Sherman, Z. de Haaff, and Z. Wang, "Structural Monitoring of Steel Member Bridge with Fatigue Life Prognosis Due to Dynamic Vehicular Loads," Georgia Institute of Technology, FHWA-GA-25-2218, Nov. 2025.

[8] J. W. Fisher and P. B. Keating, "Distortion-induced Fatigue Cracking of Bridge Details with Web Gaps," *Journal of Constructional Steel Research*, vol. 12, no. 3–4, pp. 215–228, Jan. 1989, doi: 10.1016/0143-974X(89)90056-4.

[9] J. D. Fasl, "Estimating the Remaining Fatigue Life of Steel Bridges Using Field Measurements," The University of Texas at Austin, 2013.

[10] Y.-J. Lee and S. Cho, "SHM-Based Probabilistic Fatigue Life Prediction for Bridges Based on FE Model Updating," *Sensors*, vol. 16, no. 3, pp. 1–14, Mar. 2016, doi: 10.3390/s16030317.

[11] J. R. McConnell and Y. S. J. Almoosi, "Field Evaluation of Fatigue Stresses in a Modern Highly Skewed Steel I-Girder Bridge," *J. Bridge Eng.*, vol. 27, no. 4, pp. 04022005-(1-15), Apr. 2022, doi: 10.1061/(ASCE)BE.1943-5592.0001829.

[12] S. J. Maddox, *Fatigue Strength of Welded Structures*, 2nd ed. Woodhead Publishing, 1991.

[13] J. D. Pass, K. H. Frank, and J. A. Yura, "Fatigue Behavior of Longitudinal Transverse Stiffener Intersection," Center for Transportation Research, Bureau of Engineering Research, The University of Texas at Austin, Research Report FHWA/TX-83/9+247-5F, May 1983.

[14] C. X. Li, L. Ke, Z. Y. Chen, Y. M. Xiong, and Z. Hu, "Fatigue Performance of Diaphragm Cutouts in Steel Box Girder," in *Maintenance, Safety, Risk, Management and Life-Cycle Performance of Bridges*, 1st ed., N. Powers, D. M. Frangopol, R. Al-Mahaidi, and C. Caprani, Eds., CRC Press, 2018, pp. 2446–2452. doi: 10.1201/9781315189390-331.

[15] D. Hwang, S. Kim, and H.-K. Kim, "Long-Term Damping Characteristics of Twin Cable-Stayed Bridge under Environmental and Operational Variations," *J. Bridge Eng.*, vol. 26, no. 9, p. 04021062, Sep. 2021, doi: 10.1061/(ASCE)BE.1943-5592.0001761.

[16] J. M. Caicedo, "Practical Guidelines for the Natural Excitation Technique (NExT) and the Eigensystem Realization Algorithm (ERA) for Modal Identification Using Ambient Vibration," *Experimental Techniques*, vol. 35, no. 4, pp. 52–58, Jul. 2011, doi: 10.1111/j.1747-1567.2010.00643.x.

[17] "ALDOT Works to Ensure Smooth Gameday Experience," Alabama Department of Transportation, Aug. 30, 2024. [Online]. Available: https://aldotnews.com/2024/08/30/aldot-works-to-ensure-smooth-gameday-experience/

[18] *Abaqus/CAE (2024)*. Dassault Systèmes, RI, USA.

[19] A. K. Chopra, *Dynamics of Structures: Theory and Applications to Earthquake Engineering*, 4th ed. Boston, MA: Pearson, 2012.